



UvA-DARE (Digital Academic Repository)

The origins of Calcium-rich Supernovae From Disruptions of CO white Dwarfs by Hybrid He-CO White Dwarfs

Zenati, Y.; Perets, H.B.; Dessart, L.; Jacobson-Galán, W.V.; Toonen, S.; Rest, A.

DOI

[10.3847/1538-4357/acaf65](https://doi.org/10.3847/1538-4357/acaf65)

Publication date

2023

Document Version

Final published version

Published in

Astrophysical Journal

License

CC BY

[Link to publication](#)

Citation for published version (APA):

Zenati, Y., Perets, H. B., Dessart, L., Jacobson-Galán, W. V., Toonen, S., & Rest, A. (2023). The origins of Calcium-rich Supernovae From Disruptions of CO white Dwarfs by Hybrid He-CO White Dwarfs. *Astrophysical Journal*, 944(1), Article 22. <https://doi.org/10.3847/1538-4357/acaf65>

General rights

It is not permitted to download or to forward/distribute the text or part of it without the consent of the author(s) and/or copyright holder(s), other than for strictly personal, individual use, unless the work is under an open content license (like Creative Commons).






Disclaimer/Complaints regulations

If you believe that digital publication of certain material infringes any of your rights or (privacy) interests, please let the Library know, stating your reasons. In case of a legitimate complaint, the Library will make the material inaccessible and/or remove it from the website. Please Ask the Library: <https://uba.uva.nl/en/contact>, or a letter to: Library of the University of Amsterdam, Secretariat, P.O. Box 19185, 1000 GD Amsterdam, The Netherlands. You will be contacted as soon as possible.

UvA-DARE is a service provided by the library of the University of Amsterdam (<https://dare.uva.nl>)



The Origins of Calcium-rich Supernovae From Disruptions of CO White Dwarfs by Hybrid He–CO White Dwarfs

Yossef Zenati^{1,2,7} , Hagai B. Perets² , Luc Dessart³ , Wynn V. Jacobson-Galán⁴ , Silvia Toonen⁵ , and Armin Rest^{1,6} ¹ Physics and Astronomy Department, Johns Hopkins University, Baltimore, MD, 21218, USA; yzenati1@jhu.edu, hperets@physics.technion.ac.il² Technion—Israel Institute of Technology, Physics department, Haifa 3200002 Israel³ Institut d’Astrophysique de Paris, CNRS-Sorbonne Université, 98 bis boulevard Arago, F-75014 Paris, France⁴ Department of Astronomy and Astrophysics, University of California, Berkeley, CA, 94720, USA⁵ Anton Pannekoek Institute for Astronomy, University of Amsterdam, 1090 GE Amsterdam, The Netherlands⁶ Space Telescope Science Institute, 3700 San Martin Dr., Baltimore, MD, 21218, USA

Received 2022 July 14; revised 2022 December 30; accepted 2022 December 31; published 2023 February 9

Abstract

Calcium-rich explosions are very faint ($M_B \sim -15.5$), type I supernovae (SNe) showing strong Ca lines, mostly observed in old stellar environments. Several models for such SNe have been explored and debated, but none were able to reproduce consistently the observed properties of Ca-rich SNe, nor their rates and host-galaxy distributions. Here we show that the disruptions of low-mass carbon–oxygen (CO) white dwarfs (WDs) by hybrid helium–CO (HeCO) WDs during their merger could explain the origin and properties of such SNe. We make use of detailed multidimensional hydrodynamical–thermonuclear (FLASH) simulations to characterize such explosions. We find that the accretion of CO material onto an HeCO-WD heats its He shell and eventually leads to its “weak” detonation and ejection and the production of a sub-energetic $\sim 10^{49}$ erg Ca-rich SN, while leaving the CO core of the HeCO-WD intact as a hot remnant WD, possibly giving rise to X-ray emission as it cools down. We model the detailed light curves and spectra of such explosions and find excellent agreement with the observations of Ia/c Ca-rich, and potentially Ib Ca-rich, SNe. We thereby provide a viable, consistent model for the origins of Ca-rich SNe. These findings can shed new light on the role of Ca-rich SNe in the chemical evolution of galaxies and the intracluster medium, and their contribution to the observed 511 Kev signal in the galaxy originating from positrons produced from ^{44}Ti decay. Finally, the origins of such SNe points to the key role of HeCO-WDs as SN progenitors and their potential role as progenitors of other thermonuclear SNe including normal Ia.

Unified Astronomy Thesaurus concepts: Type Ia supernovae (1728); White dwarf stars (1799); Hydrodynamical simulations (767)

1. Introduction

The discovery of the type Ib (He-rich, hydrogen-poor) SN 2005E in a remote position of an early-type galaxy, where no evidence of star-forming regions were detected lead to the detailed study and characterization of a novel type of faint Ca-rich supernovae (hereafter denoted CaSNe).

The ejected mass from such SNe was inferred to be low ($\lesssim 0.6 M_\odot$) and they are typically found in old stellar environments; in addition, their photometric and spectroscopic properties are peculiar and differ from those of typical type Ib SNe. The light curves of these typical CaSNe are characterized by a peak absolute magnitude of -14 to -16.5 mag, with fast rise times of $t_r \lesssim 15$ days (Perets et al. 2010; Kasliwal et al. 2012; Jacobson-Galán et al. 2020a). These SNe showed strong Ca II lines, leading to their original identification as Ca-rich.⁸

Many of these faint SNe showed evidence for helium lines and were identified as type Ib SNe (Perets et al. 2010), although later surveys identified faint, Ca-rich Ia/c SNe showing no clear He lines, suggesting a likely continuum of spectroscopic properties showing a range of events, from SN Ia-like features (Ca-Ia objects) to those with SN Ib/c-like features (Ca-Ib/c objects) at peak light (De et al. 2020).

Detection of such SNe is difficult, given their low luminosity and rapid evolution. However, the inferred rates of such SNe are likely in the range of 5%–20% of the normal type Ia SN rates (Perets et al. 2010; Kasliwal et al. 2012; Meng & Han 2015; De et al. 2020). The demographics of their host galaxies differ from those of normal type Ia SNe. Normal type Ia SNe are inferred to have a delay-time distribution favoring short delays, most of which exploding up to a gigayear following their stellar progenitor’s formation (Maoz et al. 2018). In contrast, the majority of CaSNe were observed in early-type galaxies, and are generally observed in old environments, far from star-forming regions (Perets et al. 2010, 2011; Kasliwal et al. 2012; Lyman et al. 2013; De et al. 2020), suggesting a much more extended delay-time distribution. CaSNe also appears to have relatively large offsets from their host galaxy nuclei (Kasliwal et al. 2010; Perets et al. 2010; Foley 2015; De et al. 2020), however, this was shown to be the result of their high frequency in early-type galaxies, in which the stellar halos are large (Perets & Beniamini 2021).

The recent discovery and detailed observations of the close-by SN 2019ehk in M100 (De et al. 2021; Nakaoka et al. 2021),

⁷ CHE Israel Excellence Fellowship.

⁸ Some studies suggested that these explosions do not in fact produce more Ca in abundance relative to O, and it has been suggested to term such SNe as Ca-strong SNe, referring to the line strength. However, in the models shown here, a large fraction of the ejecta is composed of Ca, as originally suggested (Perets et al. 2010), and we, therefore, refer to these objects as CaSNe, as originally suggested.



shed new light on the properties of such CaSNe, and in particular, gave rise to the first detection of early X-ray emission from a thermonuclear SN (Jacobson-Galán et al. 2020a; Jacobson-Galán et al. 2021).

Given these various properties showing evidence for (1) large He abundances (either directly observed, or potentially inferred from the large abundance of He-burning intermediate element products), (2) inefficient burning, leading to low production of ^{56}Ni and faint, low-luminosity SNe, and (III) old environments, we suggested that these SNe form a novel type of SN, arising from the thermonuclear explosion of He-rich white dwarfs (WDs) (Perets et al. 2010), rather than from the core collapse of massive stars (typically thought to be the progenitors of type Ib SNe).

Production of faint and CaSNe in models were already seen in the 1980s (Nomoto 1982, 1984; Woosley et al. 1986), where such SNe were produced in models of detonation of an He shell (suggested to be accreted from a companion through stable mass transfer) on CO-WDs, which failed to explode the CO-WD. These did not receive much attention as they did not produce normal type Ia SNe, nor any other type of SNe observed at the time. More recent studies further explored these models and termed such SNe Ia SNe (Bildsten et al. 2007). Following our identification and characterization of CaSNe arising from He-rich WD explosions, several models tried to reproduce the properties of CaSNe. These models explored the detonation of a massive He shell on top of low-mass CO-WDs (Shen et al. 2010; Waldman et al. 2011; Meng & Han 2015). Although such models did produce faint CaSNe they produced light curves and spectral series that were inconsistent with the observed evolution of CaSNe. Other scenarios such as a WD disrupted by a neutron star (NS) or a black hole (BH) typically produced too faint and too rapidly evolving SNe, not resembling CaSNe (Metzger 2012; Fernández & Metzger 2013; MacLeod et al. 2014; Zenati et al. 2019a, 2020a; Bobrick et al. 2021). Indeed, the later stage of NS–He WD binaries may be observed as ultracompact X-ray binaries (UCXBs) (Nelson et al. 1986; Bobrick et al. 2017). Furthermore, population synthesis models of NS–WD mergers did not produce significant long delay-time distributions that could be consistent with the significant fraction of early-type host galaxies for CaSNe (Toonen et al. 2018).

We have already proposed (Perets et al. 2019) that hybrid HeCO-WDs (Iben & Tutukov 1985; Han et al. 2007; Prada Moroni & Straniero 2009; Zenati et al. 2019b) play a key role in the production of thermonuclear SNe (Perets et al. 2019; Pakmor et al. 2021), and may produce most of the normal type Ia SNe (Perets et al. 2019). Here we propose a novel model for the origins of CaSNe, in which a hybrid HeCO-WD disrupts a low-mass CO-WD. The debris dynamically accretes on the hybrid WD, and then the CO debris mixes with the He shell of the hybrid, and detonates, while the hybrid WD core does not explode. We show that such a scenario can reproduce the overall light curves and spectra of CaSNe. We also find that large abundances of Ca and ^{44}Ti are produced. As we also discuss elsewhere, the progenitors of such disruptions give rise to a significant population of SNe with long delay times that would be observed in early-type host galaxies, as observed for CaSNe (S. Toonen et al. 2023, in preparation).

This paper is organized as follows. In Section 2 we overview the proposed scenario and its basic aspects. We then present the initial conditions and structure of the post-disruption debris

disk in our models in Section 3. In Section 4 we present the details of our numerical results, including the FLASH axisymmetric hydro-thermonuclear simulations and the radiative-transfer modeling. In Section 5 we present the disk evolutions and explosions seen in our models, and the resulting light curves and spectra. We then discuss (Section 6) our results in comparisons with observations, explore their implications, and point to potential caveats. Section 7 briefly shows the stellar populations of CaSNe followed by our summary in Section 8.

2. Disruption of a CO-WD by an HeCO-WD

Hybrid HeCO-WDs (Iben & Tutukov 1985; Han et al. 2007; Prada Moroni & Straniero 2009; Zenati et al. 2019b) are formed in interacting binaries where an evolved red giant is stripped of its hydrogen envelope (mostly) and partly stripping of its helium-rich envelope during its evolution. This complex binary evolution channel can give rise to hybrid WDs, composed of significant fractions of both CO and He. Such hybrid WDs reside in the mass range of $\sim 0.4\text{--}0.73 M_{\odot}$ and contain a He-envelope containing $\sim 2\%\text{--}20\%$ of the WD mass (Zenati et al. 2019b), with lower-mass hybrids typically containing larger He fractions (but other HeCO-formation branches might produce larger He fractions even in the high-mass range; Pakmor et al. 2021). Such hybrid WDs are frequent among compact WD–WD binaries that are inspiral and merge in a Hubble time; where 25% of all WD–WD mergers may include an HeCO-WD (Perets et al. 2019).

In a previous study, we explored the case of a CO-WDs of $>0.7 M_{\odot}$ disrupting lower-mass HeCO-WDs and eventually producing normal type Ia SNe (Perets et al. 2019). Here we investigate the cases where low-mass CO-WDs are disrupted by hybrid HeCO-WDs and show that these lead to the production of CaSNe with detailed properties matching those of observed CaSNe.

In the current models, we do not simulate the actual disruption of the lower-mass WD, which requires expensive and less-resolved 3D simulations but assume, similar to Perets et al. (2019), that it was already disrupted and formed a debris disk around the higher-mass WD. The axisymmetric disk now allows us to use a 2D model. We, therefore, introduce a disk of debris around an HeCO in a 2D axisymmetric simulation and follow the accretion evolution of the debris onto the embedded HeCO-WD. As discussed below, the accreted material eventually heats up and an He-enriched detonation ensues in the outer shell of the HeCO-WD, leading to a weak explosion, which leaves the core of the HeCO-WD intact. We then model the light curves and spectra produced from the explosion using a non-local thermodynamic equilibrium (non-LTE) 1D code CMFGEN. In the following, we discuss the various assumptions and modeling processes in more detail.

3. Initial Conditions of the Post-disruption Debris Disk

3.1. Disk Structure

We focus on disks that form when a CO-WD is tidally disrupted by a more massive HeCO-WD companion in a close binary system, and follow similar modeling of the debris disk evolution around compact objects as done by us and others in other contexts (see, Papaloizou & Pringle 1984; Fryer et al. 1999; Metzger 2012; Schwab et al. 2012; Fernández & Metzger 2013;

Bobrick et al. 2017; Zenati et al. 2019a; Perets et al. 2019; Metzger et al. 2021).

In this section, we estimate the characteristic properties of these binary mergers analytically and provide insights into the initial conditions of the debris disk, the transient WD accretion phase, and the key timescales involved. We use these analytic results to establish the initial conditions for our numerical simulations described in Section 4.

3.1.1. Disk Formation

The disruption process of the companion WD depends on the stability of the mass loss following the onset of Roche-lobe overflow (RLOF). Mass transfer occurs as the binary loses orbital angular momentum, resulting in the RLOF of the secondary onto the primary. We are interested in the fate of unstable mass transfer in a binary system consisting of an HeCO-WD primary of mass M_{WD} and radius R_{WD} orbited by a secondary CO-WD companion of mass $M_{\text{WDco}} \lesssim M_{\text{WDHeCO}}$ and radius $R_{\text{WDHeCO}} \lesssim R_{\text{WDco}}$.

The characteristic radial dimension of the disk can be estimated as (e.g., Margalit & Metzger 2016)

$$R_{\text{d},0} = a_{\text{RLOF}}(1 + q)^{-1}. \quad (1)$$

The mass of the formed disk will be about equal to the original CO-WD, $M_{\text{d},0} \approx M_{\text{WD}}^{\text{CO}}$. The stability of the mass transfer depends on the mass ratio of the binary $q = \frac{M_{\text{WD}}^{\text{CO}}}{M_{\text{WD}}^{\text{HeCO}}} = 0.83\text{--}0.88$. For circular orbits, this takes place at an orbital separation (Eggleton 1983) of

$$a_{\text{RLOF}} \approx R_{\text{WD}}^{\text{CO}} \frac{0.6q^{2/3} + \ln(1 + q^{1/3})}{0.49q^{2/3}}. \quad (2)$$

These provide us with the typical masses and scales of the formed disks. Following the disruption, the newly formed disk is very thick, as also seen in 3D models of the disruption stage (e.g., Dan et al. 2011; Raskin et al. 2012; Sato et al. 2015). The vertical scale-height H_0 and aspect ratio are typically $\theta_0 \equiv H_0/R_{\text{d},0} \sim 0.55\text{--}0.9$ (Metzger 2012; Margalit & Metzger 2016; Zenati et al. 2019a; Metzger et al. 2021). The gravity pressure is $P_* \simeq \rho c_s^2 \simeq \Sigma/2\pi h$, where Σ is the initial surface density of the disk and c_s is the sound speed.

3.1.2. Disk Stability

The formed disk evolves through accretion onto the central object, during which the disk heats up. Magnetic torques arising from the magnetorotational instability (MRI; Balbus & Hawley 1998, for post-merger magnetized evolution of a Double WD (DWD); Ji et al. 2013) likely transfer the angular momentum of the material outward in the accretion disk so that the material inspirals onto the central object (in this study the HeCO-WD). Our model does not include magnetic fields, and cannot self-consistently introduce viscous evolution to the disk. Instead, the viscous evolution is modeled through the use of artificial viscosity, following a Shakura–Sunyaev-like viscous evolution. In principle, gravitational instabilities might produce spiral arms in the disk and provide other angular momentum transfer processes (see Kashyap et al. 2015). However, the disk is likely to be stable. The Toomre (1964) stability parameter, Q ,

is given by

$$Q = \frac{\Omega c_s}{\pi G \Sigma} \Big|_{r=R_{\text{d},0}} \approx \frac{(M_{\text{WD}}^{\text{HeCO}} + M_{\text{WD}}^{\text{CO}})^2}{M_{\text{WD}}^{\text{HeCO}} M_{\text{WD}}^{\text{CO}}} \frac{H_0}{a_{\text{RLOF}}} \sim \frac{1 + q}{q} \theta_0. \quad (3)$$

For the typical disk masses and thickness, we consider here, $\theta_0 = 0.55$, $q \gtrsim 0.83\text{--}0.88$, and $Q = 1.17\text{--}1.23$, and the disk is stable. Generally, during the following evolution of the disk the viscous heating is larger than the radiative cooling, and the disk is likely to be gravitationally stable up to the point a detonation occurs. This should nevertheless be further verified in future 3D simulations. Here, using 2D simulations we assume only viscous evolution and postpone studies of other scenarios to future 3D models. In the following, we briefly describe the overall timescales and accretion rates in this process and then discuss the numerical hydrodynamical modeling in the next sections.

Let us consider the relevant timescales to which will later refer. t_{orb} is orbital time-scale

$$t_{\text{orb}} \simeq 42 \left(\frac{R_{\text{d},0}}{R_{\text{WD}}^{\text{HeCO}}} \right)^{3/2} \left(\frac{M_{\text{d},0}}{M_{\odot}} \right)^{-1/2} \text{ s}, \quad (4)$$

where the typical hybrid WD radius for the same CO-WD mass is between $[1.08\text{--}1.25] \times R_{\text{COWD}}$ (see Zenati et al. 2019b). The viscous timescale is given by

$$t_{\text{visc},0} \sim \frac{r^2}{\nu} \Big|_{R_{\text{d},0}} \text{ s}, \sim \frac{1}{\alpha} \frac{1}{\theta_0^2} \left(\frac{R_{\text{d},0}^3}{GM_{\text{WD}}^{\text{HeCO}}} \right)^{1/2} \text{ s}, \quad (5)$$

$$\sim 53.2 \text{ s} \left(\frac{\alpha}{0.1} \right)^{-1} \left(\frac{\theta_0}{0.8} \right)^{-2} \left(\frac{M_{\text{WD}}^{\text{HeCO}}}{0.63 M_{\odot}} \right)^{-0.5} \left(\frac{R_{\text{d},0}}{1.12 \times 10^9 \text{ cm}} \right)^{1.5}, \quad (6)$$

where $\nu = \alpha c_s H = \alpha r^2 \Omega_K \theta^2$ is the effective kinematic viscosity, $\Omega_K \equiv (GM_{\text{d},0}/r^3)^{1/2}$ is the Keplerian orbital frequency, $c_s \approx H \Omega_K$ is the midplane sound speed, and α parameterizes the disk viscosity (see also Section 4.1).

The viscous accretion results in a characteristic accretion rate following Shakura & Sunyaev (1973), where the characteristic peak accretion rate is approximately

$$\dot{M}_0 \sim \frac{M_{\text{d},0}}{t_{\text{visc},0}} \sim 0.1 M_{\odot} \text{ s}^{-1} \Big|_{\alpha=0.1}. \quad (7)$$

The timescale for photons to diffuse out of the disk midplane is then

$$t_{\text{diff}} \simeq \kappa_{\text{es}} \frac{\Sigma}{\sqrt{2} \pi} H_0 \simeq 1 - 7 \times 10^5 \text{ yr}, \quad (8)$$

and is typically longer than the other timescales, such that radiative cooling does not play an important role.

We, therefore, consider a stable accretion disk around the primary HeCO-WD and follow its evolution through 2D hydrodynamical simulations as we discuss below.

3.2. Disk Structure

The initial disk model can be calculated using energy and pressure considerations. The total energy in the disk is given by the combined contribution from the gravitational, thermal, and kinetic energies, $e_{\text{tot}} = E_{\text{thermal}} + E_{\text{kinetic+rotation}} + E_{\text{gravity}}$, given

by

$$e_{\text{tot}} = \frac{1}{2} \left[v_{\bar{\rho}}^2 + \frac{l_z^2}{\bar{\rho}^2} \right] - \frac{GM_{d,0}}{r} - E_g(r, \rho) + e_{\text{int}}, \quad (9)$$

where $[\bar{\rho}, z]$ are the 2D axisymmetric cylindrical coordinates, see Section 4.1. The maximum density ρ_{max} and temperature T_{max} are expected at the initial innermost part of the disk, R_0 , (in the midplane at $z=0$). At that position, the pressure gradient must vanish

$$\nabla p = 0 \text{ at } \bar{\rho} = R_0, \quad (10)$$

where $p = p(\rho, T, X_i)$ is determined either using an ideal gas plus radiation or the Helmholtz equation of state (EOS).

Our solution of the disk geometry depends on the EOS and the equilibrium of the fluid, which are dominated by the HeCO-WD potential ϕ_c , the centrifugal forces, and the specific angular momentum (Papaloizou & Pringle 1984)

$$-\frac{1}{\rho} \nabla P - \nabla \phi_c + \Omega^2 \bar{\rho} \hat{\rho} = 0. \quad (11)$$

By combining the above equation with Equation (10) and the EOS, we can deduce the general Equation (11) following (Stone et al. 1999), though see also (Fernández & Metzger 2013) and Zenati et al. (2019a)

$$\frac{P}{\rho} = \frac{(\gamma + 1)GM_c}{\gamma R_0} \left[\frac{R_0}{r} - \frac{1}{2} \left(\frac{R_0}{r \sin \theta} \right)^2 - \frac{1}{2d} \right]. \quad (12)$$

We can then use the conditions in Equations (9) and (10), and the temperature corresponding to $\frac{\gamma \mathfrak{R}_g T}{M_{d,0}} = \frac{GM_c}{R_0}$, where \mathfrak{R}_g is the gas constant. In addition we can solve for T_{max} and ρ_{max} . Following Stone et al. (1999) we normalize the torus density by ρ_{max} from Equations (9) and (10), resulting in the density distribution

$$\frac{\rho}{\rho_{\text{max}}} = \left\{ \frac{2d}{d-1} \left[\frac{R_0}{r} - \frac{1}{2} \left(\frac{R_0}{r \sin \theta} \right)^2 - \frac{1}{2d} \right] \right\}^{\frac{1}{\gamma-1}}, \quad (13)$$

where d is the torus distortion parameter, which is related to the internal energy at R_0 by

$$e_{\text{int,max}} = \frac{GM_{\text{HeCO}}}{R_0} \frac{1}{2\gamma} \frac{d-1}{d}. \quad (14)$$

Bounded torus configurations require distortion parameters of $d > 1$. Imposing the requirement of $d > 1$ for physical solutions, one can obtain d from the condition in Equation (14) using T_{max} and ρ_{max} from Equations (9) and (10). Here, we set $\gamma = 5/3$ as an initial value, and then use iterative computations of the effective adiabatic index using the Helmholtz EOS, until a steady configuration is achieved.

Note that the use of a torus model provides us with a self-consistent model, but full 3D simulations show the disk may extend all the way to the WD's surface (e.g., Yoon et al. 2007; Dan et al. 2011, 2015; Shen et al. 2012; Raskin et al. 2012; Moll & Woosley 2013; Pakmor et al. 2013, 2021; Zhu et al. 2013; Sato et al. 2015), rather than be a torus initially limited to an inner radius close to the tidal disruption radius. This might depend on the specific assumptions about viscous evolution, etc. In any case, our torus models quickly evolve and fill the inner gap to form a continuous disk down to the WD's surface

(e.g., see $t = 30$ s in Figure 2), which is more similar to the specific conditions arising from the 3D merger simulation of WDs. That being said, this is an important potential caveat. The simplified torus-turned-disk models used here are only qualitatively similar to post-merger debris disks but do not self-consistently model the exact density distribution of the debris following a disruption, which would require detailed 3D simulations. We postpone such (highly computationally expensive) 3D models to a future study. Equipped with the initial disk structure, we can now explore the evolution of the disk and its explosive outcomes.

4. Methods

We model the evolution of the debris disk through 2D thermonuclear-hydrodynamical modeling using the FLASH open code (Fryxell et al. 2000), with a 19-element nuclear network. The initial properties of the WDs and the disk compositions are calculated from stellar-evolution 1D models of HeCO-WDs (Zenati et al. 2019b), which are mapped into 2D in FLASH. We post-process the results from the explosions through a larger nuclear network using the TORCH code (Timmes & Swesty 2000) in MESA (Paxton et al. 2011, 2013, 2015, 2018). We then make use of the non-LTE radiative-transfer code CMFGEN (Hillier et al. 2012) to model the light curves and spectra arising from the modeled explosions, which we then compare to the observations. These various steps are discussed in more detail below.

The nature of our FLASH simulations is similar to those we ran earlier in other WD (or NS/BH) + disk configurations, and are described by Zenati et al. (2019a, 2020a, 2020b), Perets et al. (2019), Bobrick et al. (2021), and Metzger et al. (2021). However, the type and masses of the WDs involved and their compositions differ from our previous models, leading to very different outcomes. The modeling details are described below.

4.1. Numerical Modeling through Hydrodynamical Simulations

We simulate the evolution of the HeCO-WD merger with another low-mass CO-WD, by taking the latter to be an accretion torus around the former. As discussed above, the debris disks from the CO-WDs were modeled following the same procedure used by us earlier (Perets et al. 2019), and discussed above, where we assume the disk composition is fully mixed, and follows the composition of the disrupted CO-WD as found in our stellar-evolution models. The HeCO-WDs profiles were taken from our 1D stellar-evolution modeling using the MESA stellar-evolution code to model the density, temperature, and compositions profiles of the HeCO-WDs and CO-WDs as found in our previous study (Zenati et al. 2019b), which were then mapped to the 2D configuration in FLASH.

The initial conditions (see Table 1 for the properties of the different runs) were used to run our detailed hydrodynamical simulations, using the publicly available FLASH v4.3 code (Fryxell et al. 2000). In our models we employ the unsplit piecewise parabolic method (PPM) solver of FLASH, necessary for handling artificially generated shocks, which could spread out over a few zones by the PPM hydrodynamics solver, and otherwise might lead to unphysical burning within shocks. Our simulations are in 2D axisymmetric cylindrical coordinates $[\bar{\rho}, z]$ on a grid of size $2 \times 1 [10^{10} \text{ cm}]$, using an adaptive mesh refinement with a maximum of 12 levels (the finest) and the

Table 1
Simulation Suite

Model	M_c	M_d	α	$R_{d,0}$	M_{acc}^a	$t_{\text{visc},0}^b$	$\frac{t_{\text{det}}}{t_{\text{visc},0}}^a$
...	(M_\odot)	(M_\odot)	...	(cm)	($\frac{M_\odot}{10^2}$)	(s)	(...)
fca ₁	0.63	0.55	0.1	1.12×10^9	29	53.2	0.88
fca ₂	0.63	0.52	0.1	1.22×10^9	43	62.8	0.94
fca ₃	0.58	0.52	0.1	1.14×10^9	21	51.1	0.85
fca ₄	0.63	0.55	0.05	1.11×10^9	32	106.4	0.89

Notes.^a Total accreted material until before detonation.^b Calculated from Equation (6), assuming a disk aspect ratio of $\theta = 0.8$. Model fca₄ was not studied with tracer particles.

smallest grid cell of 15 km. We used reflective boundary conditions on the symmetry axis.

We follow similar approaches as described in other works on thermonuclear SNe (e.g., Meakin et al. 2009; Perets et al. 2019) to follow the nuclear burning and detonation throughout the evolution.

We explore four different combinations of HeCO-WD—CO-WD mergers, in which the primary HeCO-WD disrupts the secondary, a lower-mass CO-WD, forming a debris disk. Although the debris disk from the disrupted CO-WD can be initially clumpy and/or asymmetric, it rapidly evolves into a relatively symmetric accretion disk around the more massive WD before any significant nuclear burning occurs (Dan et al. 2012; Kashyap et al. 2015). We, therefore, model the mergers starting only following the formation of a symmetric debris disk around the more massive HeCO-WD in our simulations, similar to the approach used by us and others (Schwab et al. 2012; Dan et al. 2015; Fernández & Metzger 2013; Zenati et al. 2019a, 2020b) to model the mergers of WDs with WDs/NSs. Such cylindrical symmetry of the disk and the central accreting WD allows us to model the merger in 2D. Such models are highly advantageous as they allow for high-resolution simulations, with relatively little numerical expense in comparison with 3D simulations, but they still potentially capture many of the important multidimensional aspects of the merger. Each of our hydrodynamical simulations includes the self-gravity of the disk and accounts for the centrifugal force as a source term. We also include neutrino heating, though it is unlikely to play an important role in the temperatures and densities reached in our models (see Ji et al. 2013; Zenati et al. 2020b). We solve the Euler equations in axisymmetric cylindrical coordinates $[\bar{\rho}, z]$. In order not to encounter numerical issues with empty cells in the simulations, we introduce a minimal density and temperature background, which are typically taken to be $\rho_{\text{bg}} = 10^{-6} \text{ g cm}^{-3}$ and $T_{\text{bg}} = 10^3 \text{ K}$, and in any case, a density which is at least 100 times smaller than the density of the debris disk and a temperature which is at least 1000 times smaller.

In order to prevent the production of an artificial and unrealistic early detonation that may arise from insufficient numerical resolution, we applied a burning-limiter approach following Kushnir et al. (2013). We use a detailed EOS and account for self-gravity; this is included as a potential multipole expansion of up to multipole $l_{\text{max}} = 12\text{--}32$ using the new FLASH multipole solver of the disk.

We use the super time-steps method in FLASH 4.0 for calculating the adaptive time steps, which is set according to the speed-of-sound Courant–Friedrichs–Lewy (CFL) condition

with a CFL factor of 0.2. We adopt the optimal strongly stability-preserving third-order Runge–Kutta scheme.

Using FLASH we solve the equations for mass, momentum, energy, and chemical species conservation

$$\frac{\partial \rho}{\partial t} + \nabla \cdot (\rho \mathbf{v}) = 0, \quad (15)$$

$$\frac{d\mathbf{v}}{dt} = \mathbf{f}_c - \frac{1}{\rho} \nabla p + \nabla \phi, \quad (16)$$

$$\rho \frac{dl_z}{dt} = \bar{\rho} (\nabla \cdot \mathbf{T})_\phi, \quad (17)$$

$$\rho \frac{de_{\text{int}}}{dt} + p \nabla \cdot \mathbf{v} = \frac{1}{\rho \nu} \mathbf{T} : \mathbf{T} + \rho (\dot{Q}_{\text{nuc}} - \dot{Q}_\nu), \quad (18)$$

$$\frac{\partial \mathbf{X}}{\partial t} = \dot{\mathbf{X}}, \quad (19)$$

$$\nabla^2 \phi = 4\pi G \rho + \nabla^2 \phi_c, \quad (20)$$

$$\mathbf{f}_c = \frac{l_z^2}{\bar{\rho}^3} \hat{\rho}. \quad (21)$$

These include source terms for gravity, shear viscosity, nuclear reactions, and neutrino cooling. Here, \mathbf{f}_c is an implicit centrifugal source term, where l_z is the z -component of the specific angular momentum. Variables have their standard meanings: ρ , \mathbf{v} , p , e_{int} , ν , \mathbf{T} , ϕ , and $\mathbf{X} = \{X_i\}$ denote, respectively, the fluid density, poloidal velocity, total pressure, specific internal energy, fluid viscosity, viscous stress tensor for azimuthal shear, gravitational potential, and mass fractions of the isotopes X_i , with $\sum_i X_i = 1$. Furthermore, $d/dt = \partial/\partial t + \mathbf{v} \cdot \nabla$, ϕ_c denotes the HeCO-WD potential, and \dot{Q}_{nuc} and \dot{Q}_ν represent the specific nuclear heating rate due to nuclear reactions and the specific cooling rate due to neutrino emission, respectively.

We employ the Helmholtz free energy $F(\rho, T)$ in FLASH (Timmes & Arnett 1999; Timmes & Swesty 2000). The Helmholtz EOS includes contributions from partially degenerate electrons and positrons, radiation, nondegenerate ions, and corrections for Coulomb effects ($P_{\text{tot}} = P_{\text{ele}} + P_{\text{pos}} + P_{\text{ion}} + P_{\text{rad}} + P_{\text{coul}}$). The most important aspect of the Helmholtz EOS is its ability to handle thermodynamic states where radiation dominates, and under conditions of very high pressure. The contributions of both nuclear reaction and neutrino cooling (Chevalier 1989; Houck & Chevalier 1991) are included in the internal energy evolution calculations, and the Navier–Stokes equations are solved with source terms due to gravity, shear viscosity, and nuclear reactions.

As discussed earlier, since our calculations are axisymmetric and do not include magnetic fields, we cannot self-consistently account for angular momentum transport due to the MRI or non-axisymmetric instabilities (e.g., associated with self-gravity). Instead, we make the common approximation of modeling the viscosity using the α -viscosity parameterization of Shakura & Sunyaev (1973), for which the kinematic viscosity is taken to be

$$\nu_\alpha = \alpha c_s^2 / \Omega_K, \quad (22)$$

where $\Omega_K = (GM_{\text{enc}}/r^3)^{1/2}$ is the Keplerian frequency given the enclosed mass M_{enc} and c_s is the sound speed. In our models, we take either $\alpha = 0.1$ or $\alpha = 0.05$ (see Table 1) for the dimensionless viscosity coefficient. The exact α parameter that best describes such systems is not known, and others have

considered lower values (e.g., Schwab et al. 2012; Shen et al. 2012). In our previous studies of WD debris disks around NSs, which have comparable scales, we found that the changing of α , while shortening the viscous timescales, did not significantly affect the overall outcomes. Here we chose a larger α than, e.g., Schwab et al. (2012), Shen et al. (2012), and Ji et al. (2013), to allow less computational expense. Future studies should further check the sensitivity of the models to this assumption.

Nuclear burning and nucleosynthesis are followed through a 19-isotope reaction network (Chevalier 1989). It is included in the simulations following a similar approach to that employed by us and others (e.g., Meakin et al. 2009; Schwab et al. 2012; Zenati et al. 2019b, 2020a, 2020b). The nuclear network used is the FLASH α -chain network of 19 isotopes, which provides the source terms \dot{X} in Equation (19) and adequately captures the energy generated during nuclear burning \dot{Q}_{nuc} (Timmes & Swesty 2000).

We made multiple simulations with increased resolution until convergence was reached. We found a resolution of 16–20 km to be sufficient for a convergence of up to 12% in energy.

4.2. Tracer Particles and Post-processing Nucleosynthesis Modeling

We followed the nucleosynthesis processes throughout the simulation and their key role in the evolution and the nuclear burning and explosive evolution. We made use of the 19 isotope reaction network in the FLASH hydrodynamical simulation, in order to follow the dynamics and the energetics of the explosive evolution. We then made use of a larger network in post-processing to follow the detailed composition of the ejecta, and allow for detailed radiative-transfer modeling.

In order to do the post-processing analysis, we introduced 8000–20,000 passive tracer particles in the various models, to track the composition, density/entropy, and temperature of the material throughout the grid, and follow the changes in these properties, where we follow the positions and velocities of the tracer particles. The tracers were initially evenly spaced every 2×10^8 cm throughout the WD and the debris disk.

Following the 2D FLASH runs we made use of the detailed histories of the tracer particles' density and temperature to be post-processed with MESA's one-zone burner (Paxton et al. 2013, 2015). We employ a 125 isotope network that includes neutrons, and composite reactions from the JINA REACLIB database (Cyburt et al. 2010). Similar to our previous simulations, we find that the results from the larger network employed in the post-processing analysis showed less efficient nuclear burning, and gave rise to somewhat higher yields of intermediate elements at the expense of lower yields of iron elements, similar to the results seen in our previous models and other works (Dan et al. 2012; Perets et al. 2019).

The tracer particles and the large network post-processing were then used to generate the detailed density/composition profile of the ejecta at the end of the simulation. In turn, these data were used to produce detailed light curves and spectra of the explosions using the non-LTE CMFGEN radiative-transfer code (Hillier & Dessart 2012; see more details below).

4.3. Radiative-transfer Modeling

The simulations with CMFGEN are 1D and are based on angular averages of the 2D simulations performed with FLASH.

When remapping this ejecta into CMFGEN, we smooth the densities and elemental distributions to reduce any sharp gradients. The density is smoothed by convolution with a Gaussian whose standard deviation is 200 km s^{-1} . For the abundances, we smooth by running a boxcar of width $0.01 M_{\odot}$ four times through the grid. The outer ejecta are also extended by a low-density outer region with a steep density falloff in order to have an optically thin outer boundary for the radiation. The initial ejecta corresponds to an epoch soon after the hydrodynamical effects are over so that the ejecta expands ballistically. At this time of a few 100 s, we evolve the ejecta assuming no diffusion, heating by radioactive decay, and cooling from expansion until a time of two days after the explosion. At that time of two days, we remap the ejecta into CMFGEN. The radial grid typically employs 80 points.

In all simulations, radioactive decay is treated for three two-step decay chains associated with ^{56}Ni , ^{52}Fe , and ^{48}Cr (six additional decay chains were considered by Dessart & Hillier 2015 but the corresponding isotopes are not available in the present ejecta). Decay power is treated as per normal (see, for example, Dessart et al. 2012) and proper allowance is made in the non-LTE equations for nonthermal ionization and excitation, as well as the additional heating term in the energy equation. For simplicity, we compute the non-local energy deposition by solving the radiative-transfer equation with a gray absorption-only opacity to γ -rays set to $0.06 Y_e \text{ cm}^2 \text{ g}^{-1}$, where Y_e is the electron fraction.

The model atom used in this work includes the following atoms and ions: He I (40,51), He II (13,20), C I (14,26), C II (14,26), O I (30,77), O II (30,111), Ne I (70,139), Ne II (22,91), Na I (22,71), Mg II (22,65), Si I (100,187), Si II (31,59), Si III (33,61), S I (106,322), S II (56,324), S III (48,98), Ar I (56,110), Ar II (134,415), Ca I (76,98), Ca II (21,77), Ti II (37,152), Ti III (33,206), Cr II (28,196), Cr III (30,145), Cr IV (29,234), Mn II (25,97), Mn III (30,175), Fe I (44,136), Fe II (275,827), Fe III (83,698), Fe IV (51,294), Fe V (47,191), Co II (44,162), Co III (33,220), Co IV (37,314), Co V (32,387), Ni II (27,177), Ni III (20,107), Ni IV (36,200), and Ni V (46,183). In this list, the parentheses refer to the number of super levels and the number of full levels (see Hillier & Miller 1998 and Hillier & Dessart 2012 for details).

5. Results

5.1. The Disk Evolution and Thermonuclear Explosion

Our modeling begins with a debris disk assumed to have formed following the disruption of a low-mass CO-WD by a higher-mass HeCO-WD. As can be seen in Figure 1, the disk evolves viscously, and the CO-WD debris is accreted onto the HeCO-WD. The CO debris that accreted onto the outer shell of the HeCO-WD is then heated up and compressed onto the He shell of the HeCO-WD until sufficiently high temperatures and densities are reached and nuclear burning ensues. This is followed by a (weak) detonation in the He-rich material, producing nuclear-burning products (see Figure 2), and ejecting a large fraction of the burned material from the He shell of the HeCO-WD and the debris disk. The explosion ejects a few times $0.1 M_{\odot}$ of mostly burned material, composed of a significant fraction of intermediate elements and in particular 20%–30% in Ca, and produces 0.01–0.05 M_{\odot} of ^{56}Ni in the different models. We explored three pairs of WDs, and explored one of the models with a different

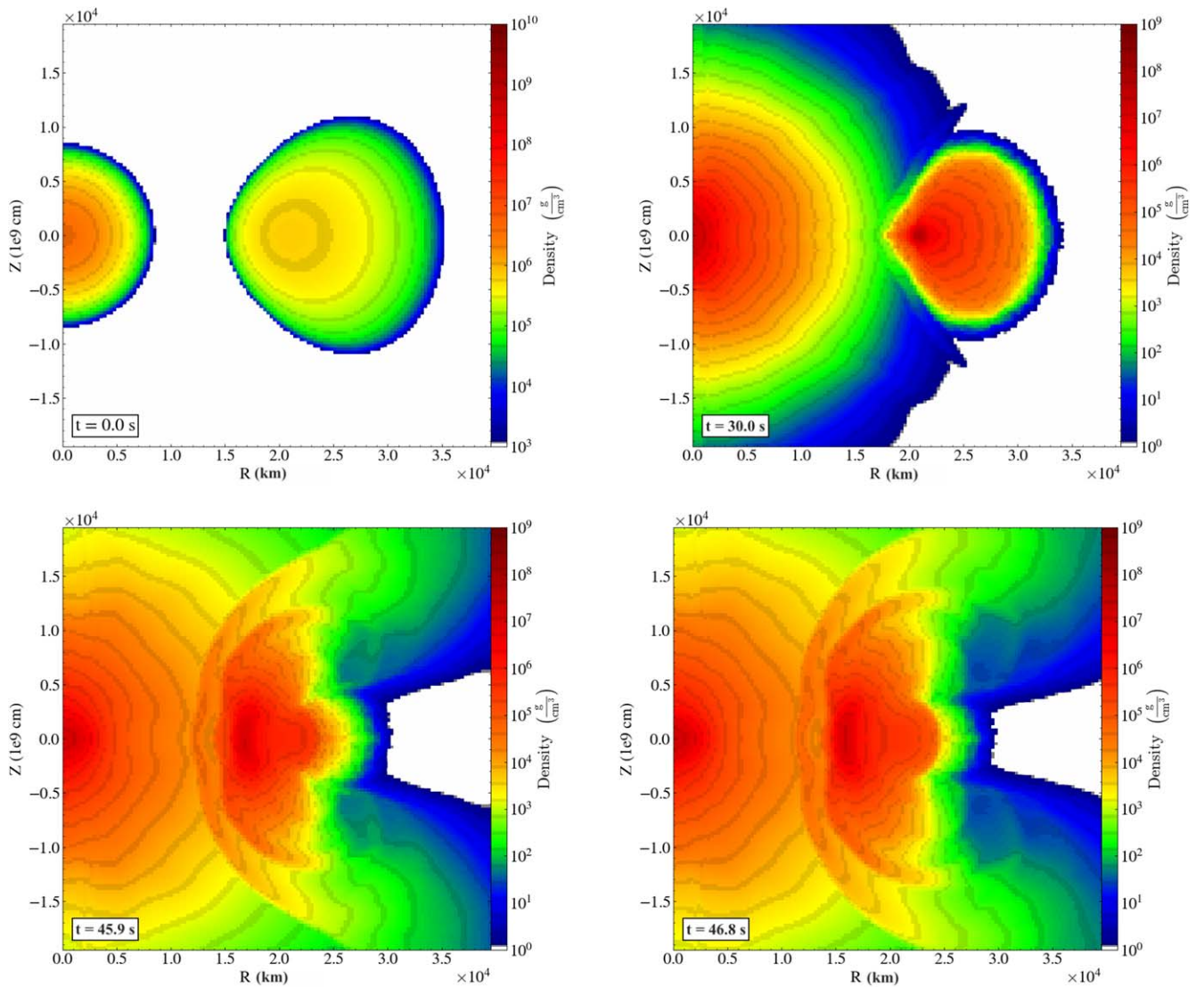


Figure 1. The evolution of the debris disk from the $0.55 M_{\odot}$ CO-WD debris disk around the HeCO-WD of mass $M = 0.63 M_{\odot}$ (see Table 1, model fca₁). The panels show the color-coded density distribution throughout the simulation. We show the initial model followed by several snapshots. Significant nuclear burning begins already at ~ 30 s (see also Figure 2), and the detonation occurs at $t_{\text{det}} \simeq 46$ s, which is about 88% of t_{visc}^0 .

viscosity parameter (but without using trace particles for the latter), for a total of four models, all showing similar accretion and nuclear-burning evolutions, but showing ranges in the specific timescales of the evolutions and the overall synthesis of nuclear-burning products. The model properties are listed in Table 1, where we also list the viscous timescale and the time of detonation in the units of the viscous timescale. The resulting ejecta, bound material, and energetics are presented in Table 2. The compositions of the ejecta in the different models are summarized in Table 3. Note that the ^{56}Ni produced differs between the models, and does not immediately show a clear correlation with the models' parameters. However, what determines the ^{56}Ni abundance is related to the amount of He-rich burnt material, and hence larger accreted material before the detonation should give rise to a larger production of ^{56}Ni . Indeed, as can be seen in Tables 1 and 2, the accretion timescale and the total mass of accreted material before the detonation are consistent with this picture, showing the ^{56}Ni mass follows the accreted material mass trend.

5.2. Light Curves and Spectra

Using the non-LTE radiation transfer code (CMFGEN), we produce the light curves and spectra resulting from each of the models. The *UBVIRJHK* LCs are shown in Figure 3. As can be seen in Figures 4 and 5, the light curves compare well with the range of observed CaSNe (not including the shock breakout early peak, likely due to CSM interactions; Jacobson-Galán et al. 2020a; also seen in X-rays, and not modeled in the current simulations). These are also compared to various other types of SNe in Figure 5. Figure 8 shows the color evolution of the models in comparison with various Ia SNe and the CaSN 2019ehk. Figure 6 shows a good comparison of the spectra with those of the CaSNe (the detailed evolution of the modeled spectra can be seen in Figures 9, 10, and 11). In Figure 12 we illustrate the ratio of $^{40}\text{Ca}/^{16}\text{O}$ of model fca₁ close to the detonation time and later, after a viscous timescale. Figure 7 shows the positions of the modeled SNe in the peak-width relation in comparison with various types of SNe, showing that the small differences in the WD masses can span a wide range of behavior, in terms of peak luminosity and the rate of

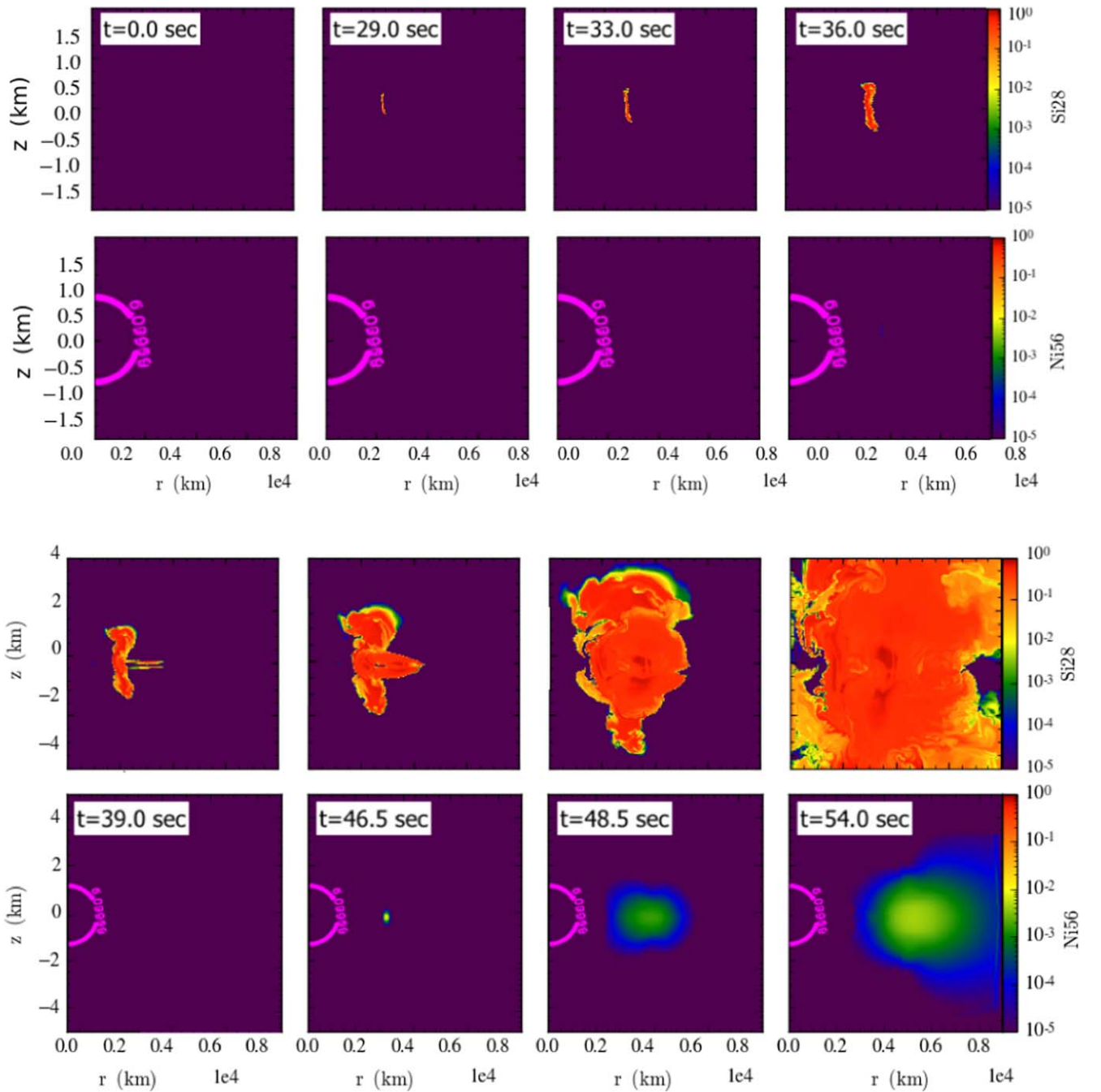


Figure 2. The evolution of model fca₁; see Table 1. The two panels show the ^{28}Si and ^{56}Ni densities as a function of time. ^{28}Si production can be first seen after $t = 0.55 t_{\text{visc}}^0$ followed by ^{56}Ni production 0.4 s after the detonation occurred. The z -axis (upper panel) shows the zoom-in fluid material. The contours show the position of the density contour of 10^6 at the beginning of the simulation.

light curve evolution. A detailed discussion of the comparison between the modeled light curves and spectra and the observations can be found in the discussion section below.

Overall, our resulting models show excellent agreement with the observed CaSNe and their ranges of properties (besides the lack of clear He lines, which are observed in many of the CaSNe; this issue is discussed below). In fact, to the best of our knowledge, these are the first models to reproduce well both the light curve and spectral evolutions of CaSNe, as well as reproduce the range of behaviors (compared with, e.g., Waldman et al. 2011 and Dessart & Hillier 2015). We should also note that the specific models were not chosen to fit any of

the observations, but rather we present all the models we ran to date.

5.3. Ejecta Composition and Line Strength

As can be seen in Tables 2 and 4, the resulting SNe produces large abundances of intermediate-group elements (IGEs) and low ^{56}Ni masses, consistent with the inefficient burning of He-rich material. In particular large fractions of the ejecta mass are composed of Ca, which gives rise to strong Ca lines. As mentioned above, it was suggested that the Ca abundances might not need to be high in CaSNe, but rather that the high nebular line ratios of Ca to O in these SNe is due to Ca being

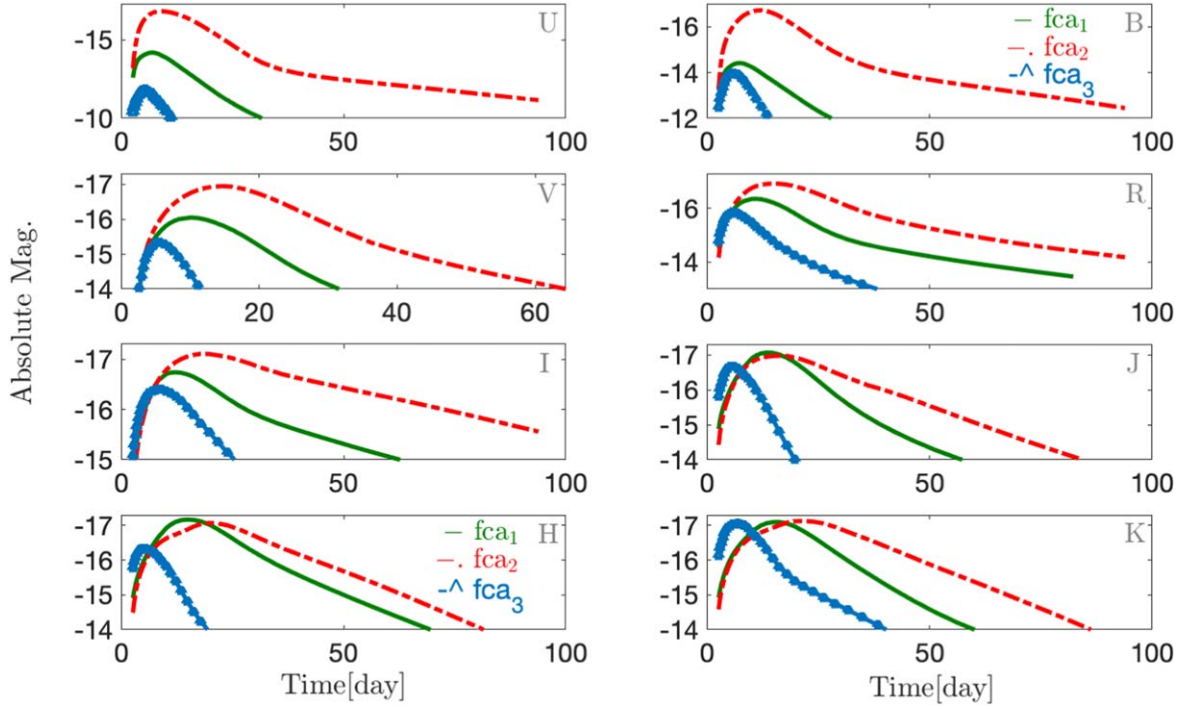


Figure 3. The light curves at different bands for the first three models in Table 1.

Table 2
CaSNe FLASH Simulation Results

Model	$M_{\text{ej}}^{\text{tot}}$ (M_{\odot})	R_{inn} (cm)	M_{bound} (M_{\odot})	M_{IMEB} $10^{-4}(M_{\odot})$	$M_{\text{IGE B}}$ $10^{-4}(M_{\odot})$	M_{unbound} (M_{\odot})	M_{IMEUB} (M_{\odot})	M_{IGEUB} (M_{\odot})	$M_{E_{\text{kin}}}$ $E_{50}(\text{erg})$
fca ₁	0.457	1.5×10^8	0.081	41.24	0.858	0.377	0.167	0.022	1.693
fca ₂	0.431	1.7×10^8	0.068	30.17	0.751	0.364	0.173	0.052	1.318
fca ₃	0.365	5.2×10^8	0.075	32.16	1.127	0.288	0.159	0.012	0.951
fca ₄	0.461	1.4×10^8	0.088	40.03	0.951	0.373	0.171	0.023	1.664

Note. The total ejecta mass was calculated after five viscous timescales (Equation (6)). We show the bound/unbound ejecta calculated as a positive Bernoulli parameter $Be > 0$. The total unbound mass is M_{unbound} . The radius R_{inn} designates the position location where the weak detonation occurred in the torus midplane. $M_{\text{IGE B}}$ and M_{IGEUB} are the bound and unbound iron group elements where the atomic number $Z \geq 23$, respectively. $M_{\text{IME B}}$ and M_{IMEUB} are bound and unbound IGEs where the atomic number $Z \geq 10$, respectively.

Table 3
Properties of the Ejecta Composition for the Models for Which the Light Curves and Spectra Were Modeled Using CMFGEN

Model	C (M_{\odot})	O (M_{\odot})	Ne (M_{\odot})	Si (M_{\odot})	Ca (M_{\odot})	Ti (M_{\odot})	^{48}Cr (M_{\odot})	^{52}Fe (M_{\odot})	^{56}Ni (M_{\odot})
fca ₁	1.01(-1)	9.91(-2)	1.24(-2)	2.32(-3)	1.40(-1)	7.97(-3)	1.01(-5)	0	2.12(-2)
fca ₂	9.38(-2)	9.09(-2)	1.17(-2)	3.34(-2)	1.09(-1)	1.48(-2)	1.97(-6)	6.86(-5)	5.00(-2)
fca ₃	8.66(-2)	1.07(-1)	5.00(-4)	8.93(-4)	1.36(-1)	7.35(-3)	3.24(-4)	5.42(-4)	1.05(-2)

Note. The number in parentheses denotes powers of ten.

such an effective coolant, and that these objects are just O-poor (Shen et al. 2019). In our models, however, the Ca abundances are inherently very high, and our successful models are indeed CaSNe, rather than just having strong Ca lines relative to O. In Figure 12 we show the spatial distributions of the ^{40}Ca and ^{16}O of model fca₁ after about one viscous timescale and at $t = 75$ s.

We do note in regard to the OI 6300 Å line strength could be sensitive to the relative fractions of Ca and O in different regions of the ejecta. In particular, the offset in abundance

between Ca and O can be very large in different regions, when the material is not well mixed (see Dessart & Hillier 2015). Since the cooling power of Ca only affects the regions where it is present, different mixing of Ca and O can potentially make large differences in the large ratios produced. In our study, we made use of a 1D non-LTE code in order to model the spectra resulting from the radiative-transfer analysis and therefore needed to map the 2D simulation data into 1D, as discussed above, potentially leading to some artificial mixing and

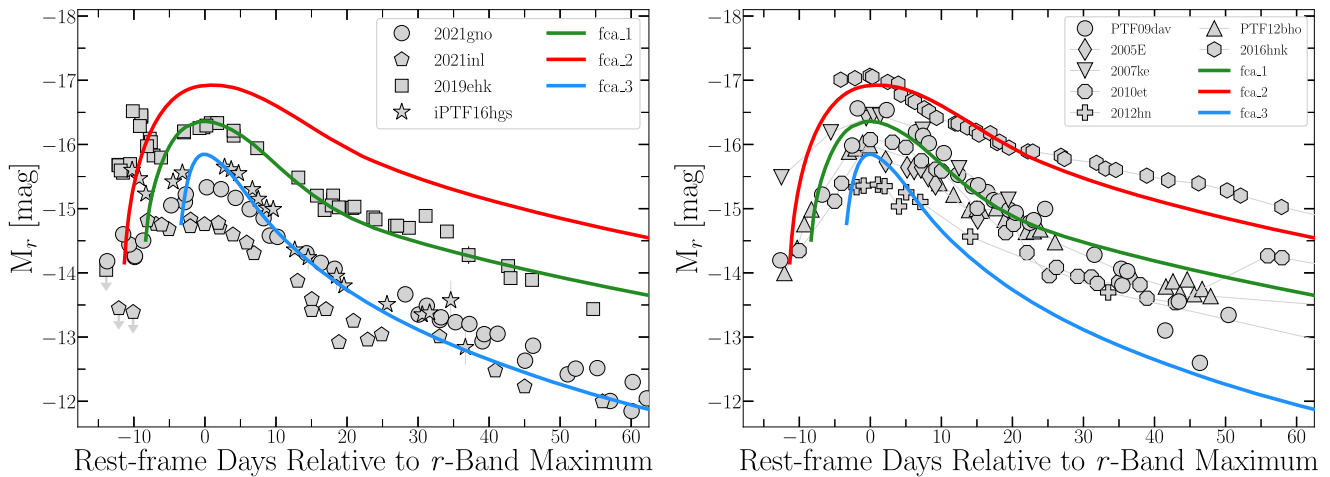


Figure 4. Left/Right: early-time absolute r -band light curves in the AB magnitude system of fca_1 (green curve), fca_2 (blue curve), and fca_3 (red curve) with respect to other classified Ca-rich transients (Perets et al. 2010; Sullivan et al. 2011; Kasliwal et al. 2012; Lunnan et al. 2017; De et al. 2018; Jacobson-Galán et al. 2020a, 2022). Peculiar, “calcium-strong” SN2016hmk (Galbany et al. 2019; Jacobson-Galán et al. 2020b) is also presented for reference (polygons). The CaSNe fca_3 model lies between the double-peaked light curves of SN 2019ehk (squares), iPTF16hgs (stars), and SN 2021gno (circle), as well as the light curve of PTF12bho (plus). Overall, the fca_2 model is most consistent with the light curve evolution of SN 2016hmk and the fca_1 model best matches SN 2019ehk’s light curve.

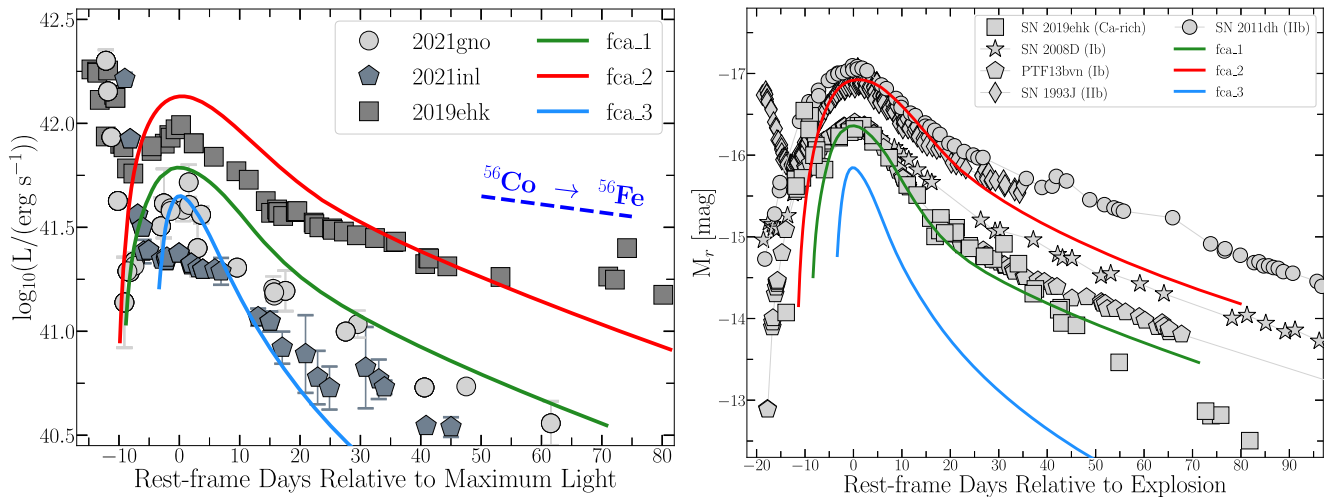


Figure 5. Left panel: the bolometric light curves from the fca_1 (green curve), fca_2 (blue curve), and fca_3 (red curve) models compared to CaSNe 2019ehk (squares), 2021gno (circles), and 2021inl (polygons). Right panel: comparison of the three models in the r -band M_r to type Ib/Ib SNe and SN 2019ehk relative to maximum light in the AB magnitude system.

composition smoothing. We therefore should note the caveat that a stronger OI 6300Å line might have been produced without such artificial mixing.

6. Discussion

Our models of the disruptions of low-mass CO-WDs by higher-mass hybrid HeCO-WDs produce faint CaSNe which agree well with the observed class of CaSNe (Perets et al. 2010), and can reproduce the range of brighter, slower-evolving CaSNe down to the fainter and faster-evolving CaSNe. In the following, we discuss in detail a comparison of the models with the observations, the various possible caveats in the models, and the overall implications of our results. We also briefly discuss the demographics of CaSNe in these contexts but postpone a more detailed discussion of the latter to a dedicated follow-up paper.

6.1. Comparison to CaSNe Observations

The fca_1 , fca_2 , and fca_3 models contain many attributes that make them consistent with the observed properties of CaSNe. In Figure 7 we present Phillip’s relation in the B band for a variety of SNe Ia, as well as some CaSNe. While both the fca_1 and fca_2 models are consistent with the decline rate ($\Delta m_{15}(B)$) for CaSNe 2007ke, PTF09dav, 2007ke, 2016hmk, and 2019ehk, the former produces a slightly fainter B -band maximum and the latter is too luminous compared to the observations. Furthermore, the fca_3 model declines much faster than these CaSNe and its maximum B -band light curve absolute magnitude is fainter, which could be consistent with some of the lowest luminosity CaSN events. Overall, the $r-i$ colors (Figure 8) of the fca_1 and fca_2 models are consistent with the observed color evolution of CaSNe; these models also show some consistency to the $B-V$ colors of the SNe Ia varieties shown in Figure 8 but are slightly bluer overall than SN 2019ehk’s evolution.

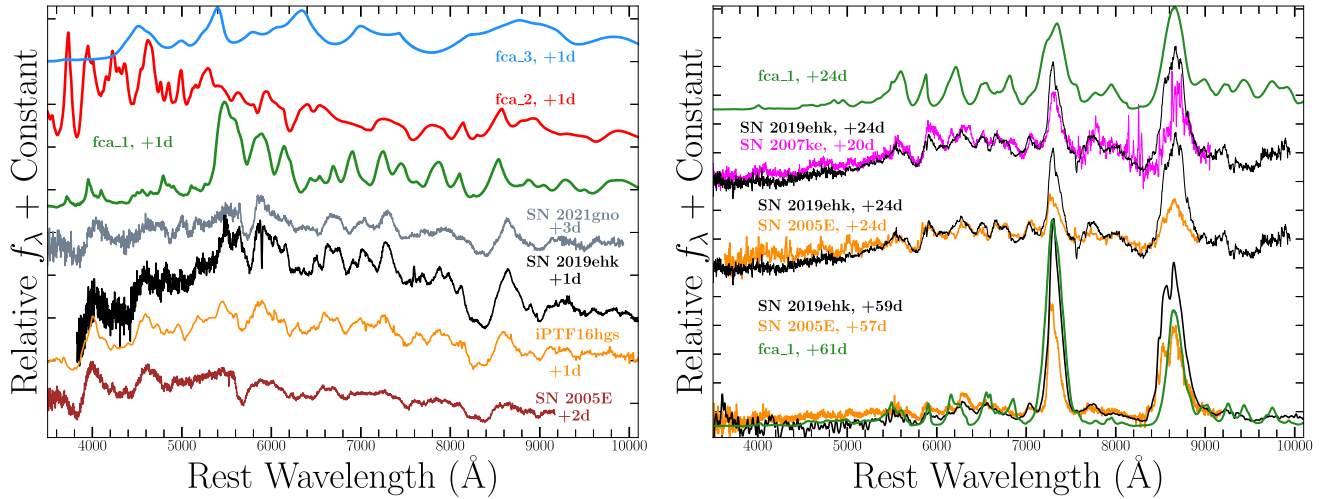


Figure 6. Left panel: early-time spectral comparison of models fca_1 (green), fca_2 (red), and fca_3 (blue) with the observations of SN 2019ehk (black) and other CaSNe at approximately the same phase. The model spectra are normalized to match the continuum of the observed Ca-rich object spectra. Right panel: direct spectral comparison of fca_1 to SN 2019ehk (black), and CaSN 2007ke (magenta), and SN 2005E (orange) at approximately the same phase. The model spectra are normalized to match the Ca II emission line profiles observed for SN 2019ehk. Almost every line transition is matched between the spectra, with our model fca_1 showing stronger [Ca II] emission than SN 2005E.

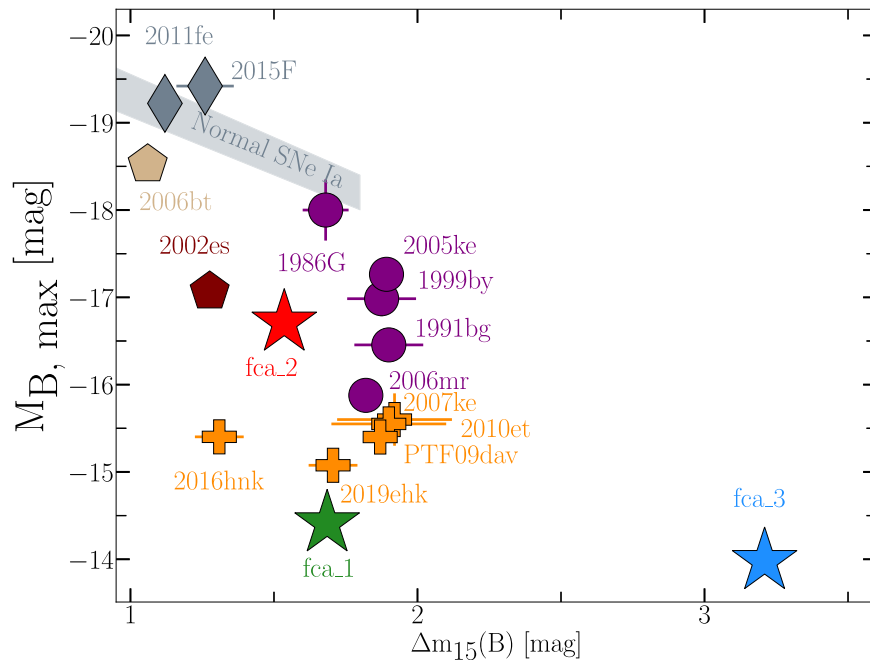


Figure 7. Illustration of Δm_{15} vs. $M_{B,\max}$ for models fca_1 (green star), fca_2 (red star), and fca_3 (blue star), and normal SNe Ia (diamonds+gray region), 91bg-like SNe Ia (circles), SNe Iax (stars), O2es-like SNe Ia (pentagons), other CaSNe (plus signs), and peculiar thermonuclear SN 2006bt (pentagon). Some uncertainties in $M_{B,\max}$ are smaller than the plotted marker sizes.

In Figure 4 we compare the r -band light curves of 10 CaSNe to the fca_1 , fca_2 , and fca_3 models. The fca_1 model provides a nearly identical match to the light curve of SN 2019ehk after the primary light curve peak, whose physical origin (e.g., circumstellar interaction or shock cooling emission) is unexplored by these models. While the evolution of the fca_2 r -band light curve matches those of the observed CaSNe, it ~ 1 – 2 mag brighter than most of the sample. However, the fca_2 model shows remarkable consistency with the peak magnitude and decline rate of the Ca-strong SN 2016hnk, which was thought to be either a 1991bg-like SN Ia (Galbany et al. 2019) or the result of an He-shell detonation of a sub-Chandrasekhar

mass WD (Jacobson-Galán et al. 2020b). Furthermore, despite its fast rise time relative to the CaSNe, the fca_3 model matches the r -band light curve peak and decline rate of a number of objects such as iPTF16hgs, SN 2005E, PTF11kmb, and SN 2021gno. The double-peaked light-curve structure is not produced in either model, however, this is expected given that this phenomenon is thought to arise with shock cooling emission or shock interaction of extended circumstellar material, as observed for iPTF16hgs, SN 2019ehk, SN 2021gno, and SN 2021inl. We note that at late times (>40 days) the luminosities of the models decline somewhat faster than the observed light curves. One possibility is that some of the newly

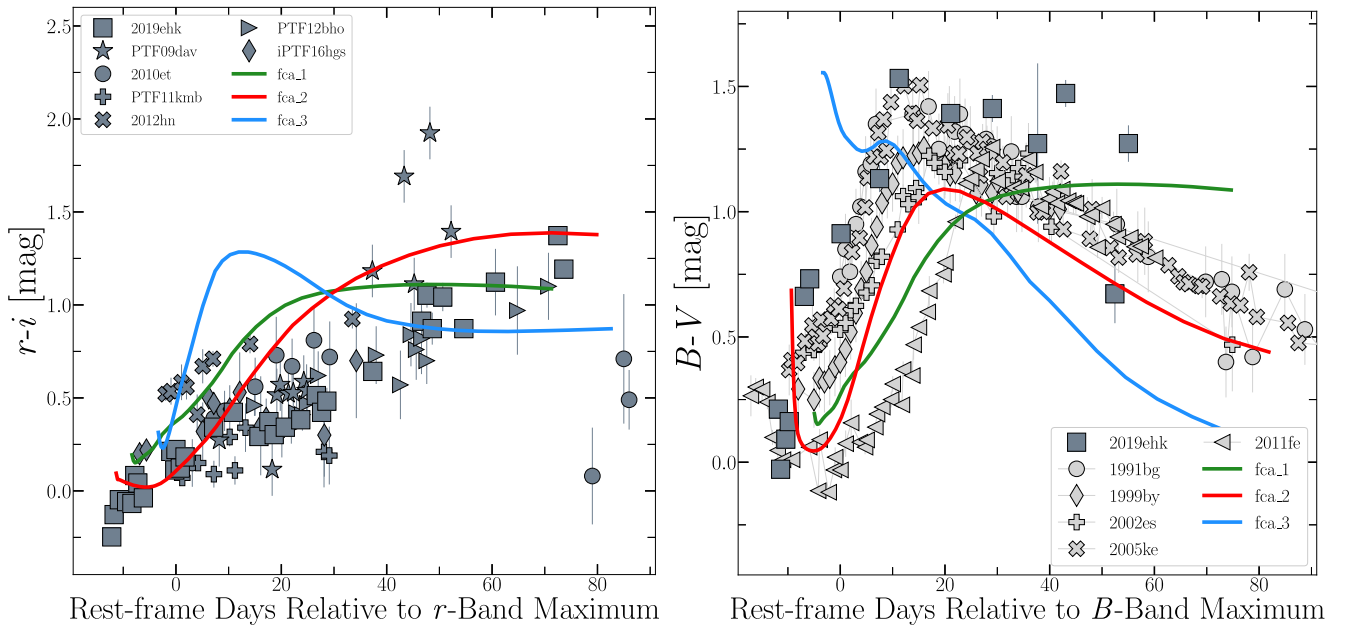


Figure 8. Color evolution comparison of models fca₁ (green curve), fca₂ (blue curve), and fca₃ (red curve) and CaSNe. Left panel: $r-i$ color comparison of models fca₁, fca₂, and fca₃ and CaSNe. Right panel: $B-V$ color comparison of the three models and various types of SNe Ia and SN 2019ehk.

Table 4
The Unbound and Bound Material of the Ejecta Masses of All Models

#	fca1 _{unbound} (M_{\odot})	fca2 _{unbound} (M_{\odot})	fca3 _{unbound} (M_{\odot})	fca1 _{bound} (M_{\odot})	fca2 _{bound} (M_{\odot})	fca3 _{bound} (M_{\odot})
¹ H	1.31×10^{-5}	4.18×10^{-5}	6.05×10^{-5}	2.77×10^{-5}	1.69×10^{-5}	2.38×10^{-5}
⁴ He	2.55×10^{-3}	9.27×10^{-4}	8.35×10^{-4}	8.47×10^{-3}	4.83×10^{-3}	3.77×10^{-3}
¹² C	1.01×10^{-1}	1.04×10^{-1}	8.84×10^{-2}	4.86×10^{-2}	5.39×10^{-2}	5.62×10^{-2}
¹⁴ N	1.69×10^{-7}	3.62×10^{-7}	1.68×10^{-6}	3.46×10^{-7}	1.45×10^{-7}	5.32×10^{-7}
¹⁶ O	9.82×10^{-2}	9.91×10^{-1}	1.55×10^{-1}	4.56×10^{-2}	2.97×10^{-2}	4.22×10^{-2}
²⁰ Ne	8.24×10^{-3}	1.12×10^{-2}	1.19×10^{-2}	3.28×10^{-5}	3.42×10^{-4}	8.48×10^{-5}
²⁴ Mg	3.17×10^{-3}	1.83×10^{-5}	5.08×10^{-5}	7.63×10^{-5}	6.33×10^{-6}	3.26×10^{-6}
²⁸ Si	2.28×10^{-3}	3.31×10^{-2}	8.89×10^{-4}	1.31×10^{-3}	1.07×10^{-3}	2.08×10^{-3}
³² S	8.23×10^{-3}	6.44×10^{-3}	2.65×10^{-3}	2.46×10^{-4}	2.61×10^{-4}	1.12×10^{-4}
³⁵ Cl	3.19×10^{-4}	3.05×10^{-4}	8.51×10^{-4}	1.62×10^{-5}	2.51×10^{-5}	1.96×10^{-5}
³⁶ Ar	6.57×10^{-4}	7.92×10^{-4}	1.99×10^{-4}	7.32×10^{-4}	1.42×10^{-4}	2.15×10^{-5}
⁴⁰ Ca	1.37×10^{-1}	1.08×10^{-1}	1.34×10^{-1}	3.06×10^{-3}	1.58×10^{-3}	8.16×10^{-4}
⁴⁴ Ti	7.94×10^{-3}	1.46×10^{-2}	7.34×10^{-3}	2.41×10^{-4}	6.03×10^{-4}	2.15×10^{-4}
⁴⁸ Cr	1.02×10^{-5}	1.94×10^{-6}	3.24×10^{-4}	4.02×10^{-6}	1.06×10^{-6}	4.52×10^{-6}
⁵² Fe	2.44×10^{-5}	7.03×10^{-5}	5.51×10^{-4}	1.16×10^{-7}	2.82×10^{-6}	4.35×10^{-5}
⁵⁴ Fe	5.29×10^{-4}	1.19×10^{-3}	1.54×10^{-3}	1.66×10^{-5}	4.59×10^{-6}	2.13×10^{-5}
⁵⁶ Ni	2.12×10^{-2}	5.05×10^{-2}	1.06×10^{-2}	5.33×10^{-5}	7.12×10^{-5}	6.02×10^{-5}

formed bound radioactive material which falls back on the WD could produce an additional radiation source, as was proposed for Iax SNe, where models suggested a WD remnant is left behind (Jordan et al. 2012; see also Kromer et al. 2013; Kawabata et al. 2021). Our radiative-transfer models include only the expanding unbound material and do not inherently include such potential contribution. The total amount of bound IGE material is, however, low (of the order of $10^{-4} M_{\odot}$ of ⁵⁶Ni, and might not be sufficient to explain the difference). Another possibility is the potentially nonspherical configuration of the ejecta, which is not accounted for by our 1D models. Last, but not least, we have only considered three mass configurations, and it is, therefore, possible that somewhat different WD masses would give rise to even more consistent results.

Additionally, the fca₂ and fca₃ models appear inconsistent with the observations of SNe IIb/Ib (Figure 5, right panel). In

terms of bolometric luminosity (Figure 5, left panel), the fca₁ and fca₂ models are consistent with the evolution of SN 2019ehk during and after its secondary light curve peak, while the fca₃ model is only consistent with SN 2021gno's peak luminosity but not its slower decline rate. However, while the fca₁ model matches the peak r -band light curve peak and decline rate of SN 2019ehk, it is not as consistent when compared to the bolometric light curve of SN 2019ehk. In Figure 5 we show that the model underpredicts the peak luminosity, declines faster than the observations, and has a faster rise time: ~ 11 days versus ~ 14 days in SN 2019ehk. Furthermore, the fca₂ bolometric light curve is similarly inconsistent with SN 2019ehk; this model overpredicts the peak luminosity and has a faster decline rate, but does have a somewhat consistent rise time of ~ 13.5 days. Nevertheless, one needs to remember that our models were not chosen as to best

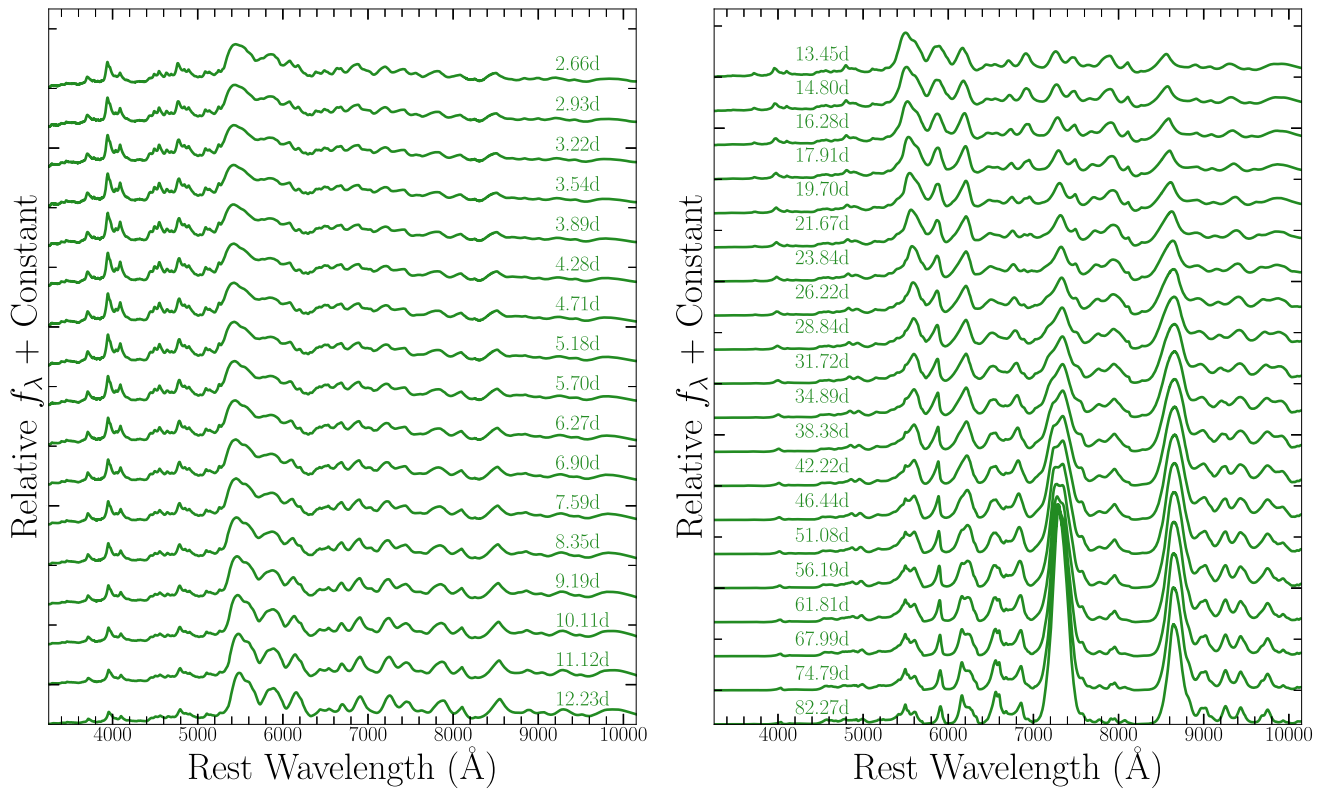


Figure 9. Spectral series of the fca_1 model. Each spectrum is normalized by the mean spectral flux.

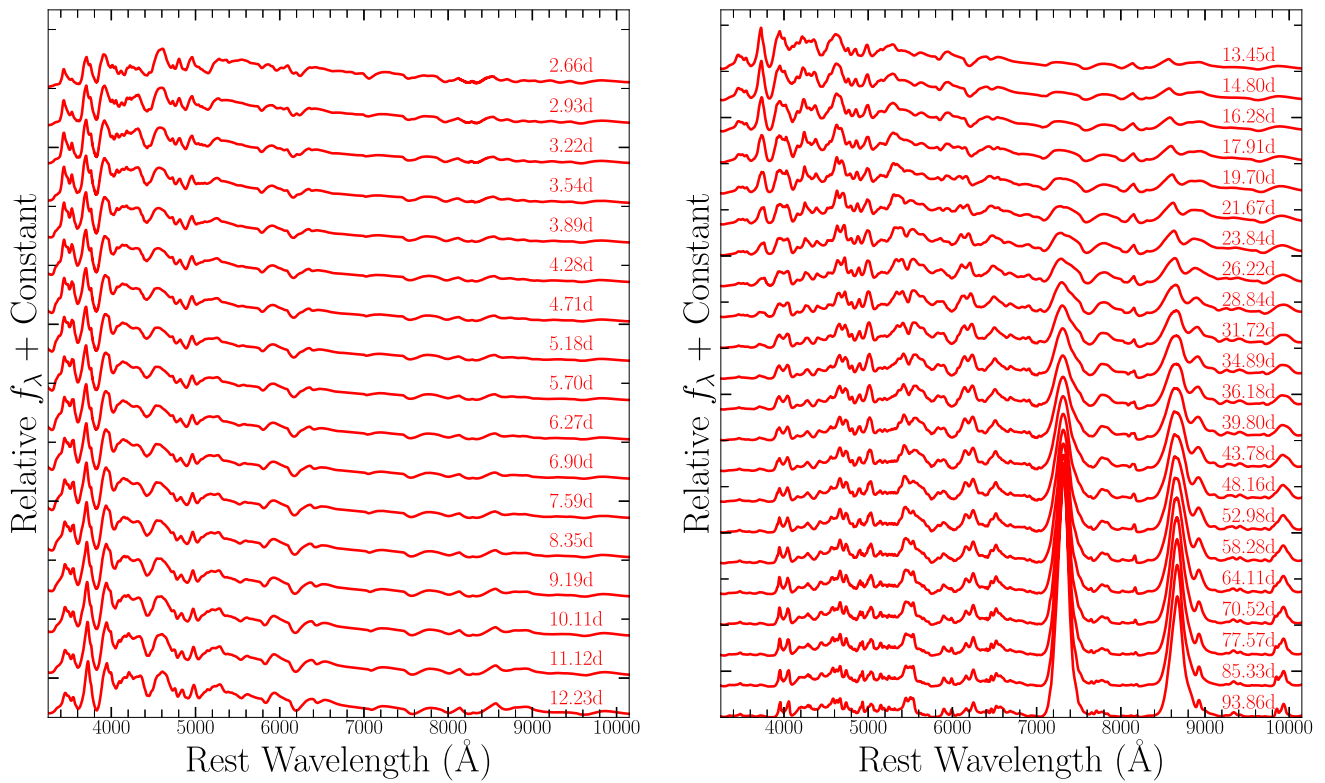


Figure 10. Spectral series of the fca_2 model. Each spectrum is normalized by the mean spectral flux.

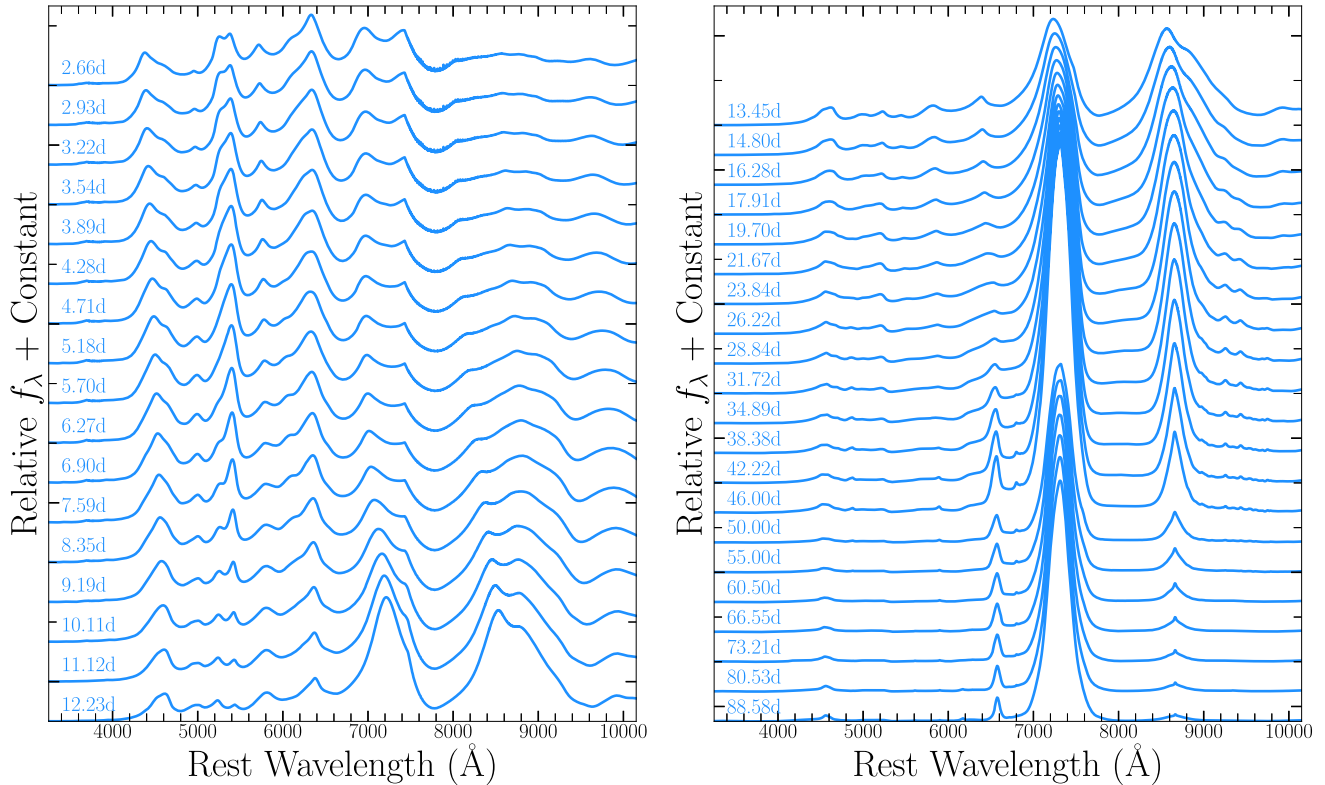


Figure 11. Spectral series of the fca_3 model. Each spectrum is normalized by the mean spectral flux.

fit the observations, but rather only to represent different regimes. A more detailed grid of models might provide models that even better reproduce the observed light curves.

In Figure 6, we present the early- and mid-time spectra of all three models relative to observed CaSNe. Near the light-curve maximum, we find that the fca_1 model shows consistent spectral features of Ca II, He I, and Si II to CaSNe and even reproduces the early-time emergence of the nebular [Ca II] transition. Furthermore, the fca_1 model spectrum is very similar to those of SNe 2005E, 2007ke, and 2019ehk at phases ~ 20 –60 days post-maximum. At this point in their evolution, both the fca_1 model and observed CaSNe spectra are dominated by Ca II emission as well as a weak [O I] emission profile, which is in line with the suggested observational definition of CaSNe that the line ratio [Ca II]/[O I] is greater than 2. Overall, the consistency of this explosion model indicates that its ejecta structure is likely very similar to that of many observed CaSNe.

6.2. He Abundances

Our HeCO-WDs are initially composed of a non-negligible He mass in the WD outer shell. However, in our current models these large He abundances existing in the initial HeCO-WDs are mostly burned, leaving only small abundances of He in the ejecta. In particular, the He contribution is too small to leave strong He spectral signatures. In that sense, our models can well reproduce He-poor CaSNe, but producing CaSNe with strong He lines could be more challenging (though one should note that the good and very secure identification of He lines in the observed case is complex; see, e.g., De et al. 2020). That being said, here we only considered a few models of HeCO-WDs disrupting CO-WDs. Other branches of HeCO-WDs could give rise to larger He abundances (see, e.g., our

discussion in Pakmor et al. 2021), and in other cases, two HeCO-WDs could merge (as we find in population synthesis modeling; to be discussed in a later paper). In both these cases, larger He abundances are available during the disruption and explosion, potentially leaving behind much larger He abundances in the ejecta. In particular, in a preliminary model where we studied the disruption of an HeCO-WD by another HeCO-WD (not shown here) using similar methods, we found that the ejecta has similar IGE, somewhat lower IME abundances, but far larger He abundances in the ejecta ($M(\text{He}) \gtrsim 7 \times 10^{-2} M_\odot$ and $M(^{40}\text{Ca}) \sim 0.08$ – $0.12 M_\odot$). This model and other more He-rich models will be discussed in a dedicated paper (Zenati, Perets, et al. 2023, in preparation). It is therefore possible that the He-strong CaSNe arise from a very similar channel but from more He-rich mergers due to double HeCO-WDs or more He-rich HeCO-WDs.

6.3. High Production of Ca ^{44}Ti and the Contribution of Positrons to the Galactic 511 keV Emission

^{44}Ti is produced from the fusion of an α -nuclei with ^{40}Ca atoms. The excessive production of ^{44}Ti is therefore typically accompanied by the excessive production of other intermediate- α elements. Highly fine-tuned conditions are therefore required in order to produce large abundances of one of these isotopes without producing significant abundances of the other. Indeed, the fractional ratio of ^{44}Ti to stable calcium, ^{40}Ca , is found to be large in all studied cases of helium detonations. Already the original identification and characterization of CaSNe as thermonuclear SNe infer large abundances of Ca, with an estimated mass of $\sim 0.1 M_\odot$ of calcium in SN 2005E, the prototype SN for this type of SNe. CaSNe are therefore likely candidates as significant production sites of ^{44}Ti . By

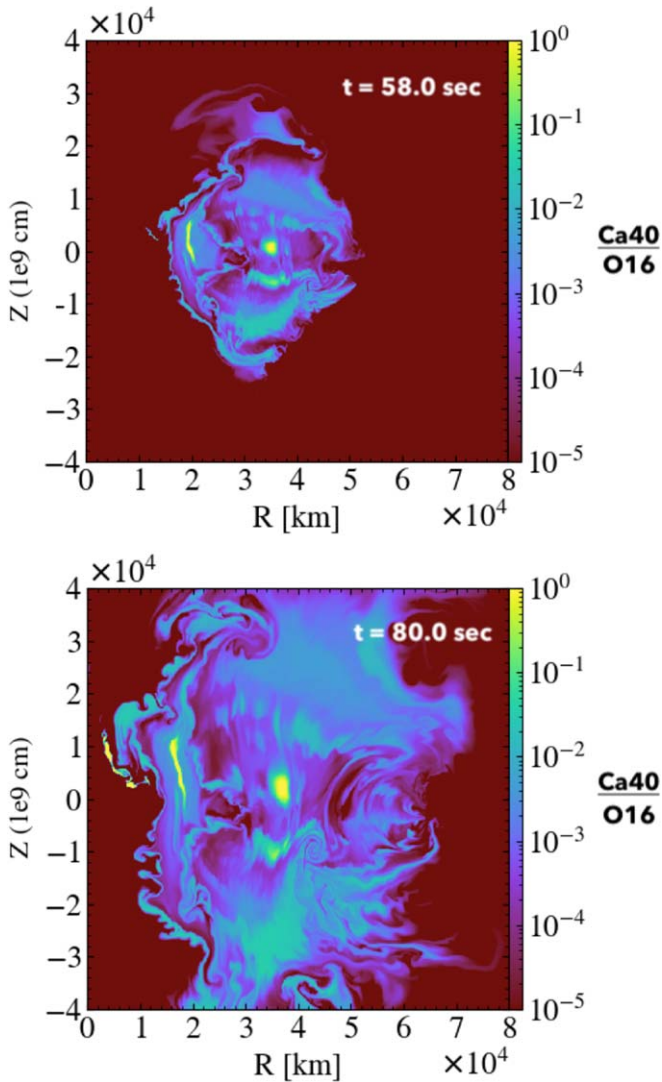


Figure 12. The spatial distribution of the ratio of $^{40}\text{Ca}/^{16}\text{O}$ at different early and late times for the fca_j model.

taking the range of ^{44}Ti to ^{40}Ca ratios found in theoretical models and the estimated calcium mass in SN 2005E one can infer that large ^{44}Ti abundances should be produced.

While some of the previous models have indeed shown a large production of Ca (Waldman et al. 2011), they did not well reproduce the observed light curves. The simulations shown here do provide a potentially successful model for CaSNe. The compositions of the ejecta from these models are shown in Table 4. As can be seen, Ca is indeed excessively produced in these models and as much as 20%–30% of the ejecta is composed of Ca, supporting the identification of 2005E-like SNe as CaSNe, rather than SNe with strong Ca lines, as mentioned above. Furthermore, our models show a significant production of ^{44}Ti with as much as $1\text{--}8 \times 10^{-2} M_{\odot}$ of ejected ^{44}Ti . In Perets et al. (2010) and Perets (2014) we suggested that the positrons produced through the later radioactive decay of ^{44}Ti in CaSNe could provide a major contribution to the Galactic 511 Kev emission, whose origins are still not understood. Perets (2014) assumed the ^{44}Ti fractions produced in CaSNe followed the results for Waldman et al. (2011)’s models, which were 1–2 orders of magnitude smaller than those found in our current models. The even larger ^{44}Ti

abundances found here suggest a potentially even more important contribution of CaSNe to 511 keV productions, even if the rate of CaSNe in the Galactic bulge is smaller than those assumed by Perets (2014).

The large abundances of Ca initially inferred from observations (Perets et al. 2010) were suggested to play an important role in explaining the origins of enhanced Ca abundances in the intracluster medium (Perets et al. 2010; Mulchaey et al. 2014). The possibility that these SNe are only Ca strong-lined rather than inherently Ca-rich (Shen et al. 2019) could potentially exclude this Ca-enrichment scenario. However, our current results do support the large Ca production, and hence their potential role in explaining the composition of the intracluster medium.

6.4. Polarization

Our radiative-transfer calculations do not model polarization, and we therefore cannot directly provide any predictions in this regard. Nevertheless, we point out that our models produce non-spherical-symmetric explosions, unlike our Perets et al. (2019) model and others’ models for normal type Ia SNe, which are typically quite spherical (see Soker 2019, Table 1). Polarization measurements of type Ia SNe show them not to be polarized (or very weakly polarized) consistent with the various suggested models. We hypothesize that the asphericity of our models for CaSNe would give rise to polarized radiation. Polarization measurements are typically quite difficult and require significant fluxes, but future polarization measurements of sufficiently close-by CaSNe might be possible, and could test this prediction, and, if correct, show them to be far more polarized than normal type Ia SNe.

6.5. Possible Caveats

While potentially providing the first successful model for CaSNe, one needs to consider several potential caveats:

1. Our models are axisymmetric 2D models, and in particular, do not consider the early disruption stage. Our disk models are therefore not directly derived from self-consistent modeling of the disk formation, which might differ from the hypothesized disk used in our models.
2. Our radiative-transfer modeling is 1D, while the explosion is likely non-spherical-symmetric, and 2D or better 3D radiative-transfer modeling might be required in order to represent better the predicted light curves and spectra.
3. The viscous evolution of our disks is modeled simplistically through an artificial Shakura–Sunayev viscosity and a more realistic evolution could potentially affect the results.
4. While our models provide a good match for CaSNe, they poorly reproduce He lines compare to those observed for many CaSNe, suggesting more He should exist in the ejecta (though, as we briefly discuss, this issue might be alleviated with HeCO–HeCO–WD mergers of more He-enriched HeCO–WDs).

Future 3D modeling of mergers (currently in progress) and 3D radiative-transfer models might resolve the first two issues, and extending our models to double HeCO–WDs (in progress) and more He-enriched HeCO–WDs would allow us to test the possibility of producing more He-rich CaSNe.

In regards to the viscosity, we have run one of the models with a different viscosity parameter, as to get a handle of its influence (see Table 1). The resulting evolution, explosion energetics, and composition, while somewhat quantitatively different than the original model, do show similar qualitative behavior, providing support to the robustness of the results in this regard. Nevertheless, more realistic simulations of this issue could better test this.

7. CaSNe Demographics and Environments

CaSNe are observed both in early-type and late-type galaxies, but they are far more abundant in early-type galaxies compared with normal type Ia SNe (e.g., Perets et al. 2010; Kasliwal et al. 2012; Lyman et al. 2013; De et al. 2020), and typically explode far from star-forming regions, suggesting a much older progenitor population for these SNe (Perets et al. 2010, 2011; Lyman et al. 2013). Such SNe are also observed in relatively large offsets from their host galaxy nuclei when observed in early-type galaxies (Perets et al. 2010; Perets 2014; Foley 2015; Perets & Beniamini 2021), consistent with the existence of large old stellar populations in the large halos of early-type galaxies (Perets & Beniamini 2021). Together, these suggest an overall delay-time distribution far more skewed toward long gigayear delays compared with normal type Ia SNe. Assuming that hybrid HeCO-WDs disrupting lower-mass WDs are the progenitors of CaSNe, as suggested here, one can explore the rates of such SNe and their delay-time distributions using population synthesis studies. The data in our original population synthesis study (Perets et al. 2019) included information on such progenitors; analyzing these data we found that such progenitors can produce rates as large as a few up to 15% of the normal type Ia rate and can have very long delays, far more extended than normal type Ia SNe. These are potentially consistent with the observed rates and demographics of CaSNe. However, these could be sensitive to the exact choice of the mass limits of the HeCO and CO-WD progenitors, the metallicities, etc. We, therefore, postpone any detailed exploration of these issues to a dedicated paper (S. Toonen et al. 2023, in preparation).

8. Summary

When we first characterized CaSNe as belonging to a unique novel type of faint, Ca- and He-rich SNe, we found many of them explode in very old environments (Perets et al. 2010), and inferred them to have low-mass ejecta. These findings already excluded a core-collapse origin for at the majority of these SNe, and pointed to a likely thermonuclear origin, arising from an He-rich explosion of a WD. Extensive observational studies of these SNe over the last decade far improved and extended our understanding of their properties. It showed them to be more diverse than originally thought (Kasliwal et al. 2012; De et al. 2020), and include He-poor (type Ia/c) SNe, and the existence of early CSM interactions (Jacobson-Galán et al. 2020a). Less progress was done on the theoretical understanding of these SNe.

Decades ago (Woosley et al. 1986) found that detonation of large He shells on low-mass WDs (suggested to form following long-term mass transfer onto a WD from a stellar companion) might produce ^{56}Ni -poor SNe, and possibly CaSNe. These were not likely to resemble normal type Ia SNe, and, consequently, they attracted little interest and follow-up studies

at the time (although they were suggested to be related to the rapidly evolving SNe 1885A and 1939B; de Vaucouleurs & Corwin 1985; Perets et al. 2011).

The finding and characterization of the novel and faint CaSNe (Perets et al. 2010) renewed interest in such He-shell detonation models, together with more modern incarnations of the (Nomoto 1982; Woosley et al. 1986), termed. Ia SNe (Bildsten et al. 2007) which considered large He-shell detonation models. These models, and new ones that produced for the first time detailed light curves and spectra of such scenarios, while having some success in producing the observed and/or inferred properties of CaSNe, did not well reproduce their overall properties (Waldman et al. 2011; Dessart & Hillier 2015). Suggestions of NS mergers with WDs were also explored as possible progenitors (Fernández & Metzger 2013), but more detailed studies of such explosions excluded these as potential progenitors for CaSNe (Toonen et al. 2018; Zenati et al. 2019a).



Here we proposed a novel model for the origin of CaSNe from the disruption of low-mass CO-WDs by hybrid HeCO-WDs, and the subsequent accretion of the CO-WD debris on the HeCO-WD. We made use of 2D hydrodynamical-thermonuclear simulations of the evolution of the debris disk and showed a weak He-rich detonation ensues following the accretion of CO material onto the HeCO He shell (surface). This weak explosion ejects a few $0.1 M_{\odot}$ of IGE-rich material and produces up to a few $0.01 M_{\odot}$ of ^{56}Ni . Using nucleosynthesis post-processing and non-LTE radiation-transport simulations, we modeled the light curves and spectra of such explosions and showed them to well match the light curves and spectra of CaSNe.

We modeled three different HeCO-WD CO-WD pairs, which produce a range of Ca-rich explosive transients, providing the best models to date for the light curves and spectra of CaSNe, and potentially explaining the range of observed CaSNe (those not showing clear He lines). We suggest that the models of double HeCO-WD mergers and/or more enriched HeCO-WDs might also produce CaSNe with more pronounced He lines.

Y.Z. thanks Kevin Schlaufman and Colin Norman for the helpful discussions. Y.Z. and H.B.P. acknowledge support for this project from the European Union’s Horizon 2020 research and innovation program under grant agreement No 865932-ERC-SNeX. W.J.-G. is supported by the National Science Foundation Graduate Research Fellowship Program under grant No. DGE-1842165. W.J.-G. acknowledges support through NASA grants in support of Hubble Space Telescope programs GO-16075 and 16500. The FLASH simulations were performed on the Astric computer cluster of the Israeli I-CORE center. The plots in this paper have been generated using Matplotlib (Hunter 2007) and yt-project (Turk et al. 2011).

Software: Astropy (Astropy Collaboration et al. 2018), NumPy (Harris et al. 2020), FLASH (Fryxell et al. 2000), TORCH (Timmes & Swesty 2000), MESA (Paxton et al. 2011, Paxton15, Paxton13, Paxton18), CMFGEN (Hillier et al. 2012), Matplotlib (Hunter 2007) and yt-project (Turk et al. 2011).

ORCID iDs

Yossef Zenati  <https://orcid.org/0000-0002-0632-8897>
 Hagai B. Perets  <https://orcid.org/0000-0002-5004-199X>
 Luc Dessart  <https://orcid.org/0000-0003-0599-8407>

Wynn V. Jacobson-Galán  <https://orcid.org/0000-0002-3934-2644>

Silvia Toonen  <https://orcid.org/0000-0002-2998-7940>

Armin Rest  <https://orcid.org/0000-0002-4410-5387>

References

- Astropy Collaboration, Price-Whelan, A. M., Sipőcz, B. M., et al. 2018, *AJ*, 156, 123
- Balbus, S. A., & Hawley, J. F. 1998, *RvMP*, 70, 1
- Bildsten, L., Shen, K. J., Weinberg, N. N., & Nelemans, G. 2007, *ApJL*, 662, L95
- Bobrick, A., Davies, M. B., & Church, R. P. 2017, *MNRAS*, 467, 3556
- Bobrick, A., Zenati, Y., Perets, H. B., Davies, M. B., & Church, R. 2021, *MNRAS*, 454, 4411
- Chevalier, R. A. 1989, *ApJ*, 346, 847
- Cybur, R. H., Amthor, A. M., Ferguson, R., et al. 2010, *ApJS*, 189, 240
- Dan, M., Guillochon, J., Brügggen, M., Ramirez-Ruiz, E., & Rosswog, S. 2015, *MNRAS*, 454, 4411
- Dan, M., Rosswog, S., Guillochon, J., & Ramirez-Ruiz, E. 2011, *ApJ*, 737, 89
- Dan, M., Rosswog, S., Guillochon, J., & Ramirez-Ruiz, E. 2012, *MNRAS*, 422, 2417
- De, K., Fremling, U. C., Gal-Yam, A., et al. 2021, *ApJL*, 907, L18
- De, K., Kasliwal, M. M., Cantwell, T., et al. 2018, *ApJ*, 866, 72
- De, K., Kasliwal, M. M., Tzanidakis, A., et al. 2020, *ApJ*, 905, 58
- de Vaucouleurs, G., & Corwin, H. G., Jr. 1985, *ApJ*, 295, 287
- Dessart, L., & Hillier, D. J. 2015, *MNRAS*, 447, 1370
- Dessart, L., Hillier, D. J., Li, C., & Woosley, S. 2012, *MNRAS*, 424, 2139
- Eggleton, P. P. 1983, *ApJ*, 268, 368
- Fernández, R., & Metzger, B. D. 2013, *ApJ*, 763, 108
- Foley, R. J. 2015, *MNRAS*, 452, 2463
- Fryer, C. L., Woosley, S. E., Herant, M., & Davies, M. B. 1999, *ApJ*, 520, 650
- Fryxell, B., Olson, K., Ricker, P., et al. 2000, *ApJS*, 131, 273
- Galbany, L., Ashall, C., Hoeflich, P., et al. 2019, *A&A*, 630, A76
- Han, Z., Podsiadlowski, P., & Lynas-Gray, A. E. 2007, *MNRAS*, 380, 1098
- Harris, C. R., Millman, K. J., van der Walt, S. J., et al. 2020, *Natur*, 585, 357
- Hillier, D. J., & Dessart, L. 2012, *MNRAS*, 424, 252
- Hillier, D. J., Dessart, L., & Li, C. 2012, in *From Interacting Binaries to Exoplanets: Essential Modeling*, ed. M. T. Richards & I. Hubeny, Vol. 282 (Cambridge: Cambridge Univ. Press), 251
- Hillier, D. J., & Miller, D. L. 1998, *ApJ*, 496, 407
- Houck, J. C., & Chevalier, R. A. 1991, *ApJ*, 376, 234
- Hunter, J. D. 2007, *CSE*, 9, 90
- Iben, I., Jr., & Tutukov, A. V. 1985, *ApJS*, 58, 661
- Jacobson-Galán, W., Venkatraman, P., Margutti, R., et al. 2022, *ApJ*, 932, 58
- Jacobson-Galán, W. V., Margutti, R., Kilpatrick, C. D., et al. 2020a, *ApJ*, 898, 166
- Jacobson-Galán, W. V., Polin, A., Foley, R. J., et al. 2020b, *ApJ*, 896, 165
- Jacobson-Galán, W. V., Margutti, R., Kilpatrick, C. D., et al. 2021, *ApJL*, 908, L32
- Ji, S., Fisher, R. T., García-Berro, E., et al. 2013, *ApJ*, 773, 136
- Jordan, G. C., Perets, H. B., Fisher, R. T., & van Rossum, D. R. 2012, *ApJL*, 761, L23
- Kashyap, R., Fisher, R., García-Berro, E., et al. 2015, *ApJL*, 800, L7
- Kasliwal, M. M., Kulkarni, S. R., Gal-Yam, A., et al. 2010, *ApJ*, 723, L98
- Kasliwal, M. M., Kulkarni, S. R., Gal-Yam, A., et al. 2012, *ApJ*, 755, 161
- Kawabata, M., Maeda, K., Yamanaka, M., et al. 2021, *PASJ*, 73, 1295
- Kromer, M., Fink, M., Stanisev, V., et al. 2013, *MNRAS*, 429, 2287
- Kushnir, D., Katz, B., Dong, S., Livne, E., & Fernández, R. 2013, *ApJL*, 778, L37
- Lunnan, R., Kasliwal, M. M., Cao, Y., et al. 2017, *ApJ*, 836, 60
- Lyman, J. D., James, P. A., Perets, H. B., et al. 2013, *MNRAS*, 434, 527
- MacLeod, M., Goldstein, J., Ramirez-Ruiz, E., Guillochon, J., & Samsing, J. 2014, *ApJ*, 794, 9
- Maaz, D., Hallakoun, N., & Badenes, C. 2018, *MNRAS*, 476, 2584
- Margalit, B., & Metzger, B. D. 2016, *MNRAS*, 461, 1154
- Meakin, C. A., Seitenzahl, I., Townsley, D., et al. 2009, *ApJ*, 693, 1188
- Meng, X., & Han, Z. 2015, *A&A*, 573, A57
- Metzger, B. D. 2012, *MNRAS*, 419, 827
- Metzger, B. D., Zenati, Y., Chomiuk, L., Shen, K. J., & Strader, J. 2021, *ApJ*, 923, 100
- Moll, R., & Woosley, S. E. 2013, *ApJ*, 774, 137
- Mulchaey, J. S., Kasliwal, M. M., & Kollmeier, J. A. 2014, *ApJL*, 780, L34
- Nakaoka, T., Maeda, K., Yamanaka, M., et al. 2021, *ApJ*, 912, 30
- Nelson, L. A., Rappaport, S. A., & Joss, P. C. 1986, *ApJ*, 304, 231
- Nomoto, K. 1982, *ApJ*, 253, 798
- Nomoto, K. 1984, *ApJ*, 277, 791
- Pakmor, R., Kromer, M., Taubenberger, S., & Springel, V. 2013, *ApJL*, 770, L8
- Pakmor, R., Zenati, Y., Perets, H. B., & Toonen, S. 2021, *MNRAS*, 503, 4734
- Papaloizou, J. C. B., & Pringle, J. E. 1984, *MNRAS*, 208, 721
- Paxton, B., Bildsten, L., Dotter, A., et al. 2011, *ApJS*, 192, 3
- Paxton, B., Cantiello, M., Arras, P., et al. 2013, *ApJS*, 208, 4
- Paxton, B., Marchant, P., Schwab, J., et al. 2015, *ApJS*, 220, 15
- Paxton, B., Schwab, J., Bauer, E. B., et al. 2018, *ApJS*, 234, 34
- Perets, H. B. 2014, arXiv:1407.2254
- Perets, H. B., Badenes, C., Arcavi, I., Simon, J. D., & Gal-yam, A. 2011, *ApJ*, 730, 89
- Perets, H. B., & Beniamini, P. 2021, *MNRAS*, 503, 5997
- Perets, H. B., Zenati, Y., Toonen, S., & Bobrick, A. 2019, arXiv:1910.07532
- Perets, H. B., Gal-Yam, A., Mazzali, P. A., et al. 2010, *Natur*, 465, 322
- Prada Moroni, P. G., & Straniero, O. 2009, *A&A*, 507, 1575
- Raskin, C., Scannapieco, E., Fryer, C., Rockefeller, G., & Timmes, F. X. 2012, *ApJ*, 746, 62
- Sato, Y., Nakasato, N., Tanikawa, A., et al. 2015, *ApJ*, 807, 105
- Schwab, J., Shen, K. J., Quataert, E., Dan, M., & Rosswog, S. 2012, *MNRAS*, 427, 190
- Shakura, N. I., & Sunyaev, R. A. 1973, *A&A*, 24, 337
- Shen, K. J., Bildsten, L., Kasen, D., & Quataert, E. 2012, *ApJ*, 748, 35
- Shen, K. J., Kasen, D., Weinberg, N. N., Bildsten, L., & Scannapieco, E. 2010, *ApJ*, 715, 767
- Shen, K. J., Quataert, E., & Pakmor, R. 2019, *ApJ*, 887, 180
- Soker, N. 2019, *NewAR*, 87, 101535
- Stone, J. M., Pringle, J. E., & Begelman, M. C. 1999, *MNRAS*, 310, 1002
- Sullivan, M., Kasliwal, M. M., Nugent, P. E., et al. 2011, *ApJ*, 732, 118
- Timmes, F. X., & Arnett, D. 1999, *ApJS*, 125, 277
- Timmes, F. X., & Swesty, F. D. 2000, *ApJS*, 126, 501
- Toomre, A. 1964, *ApJ*, 139, 1217
- Toonen, S., Perets, H. B., Igoshev, A. P., Michaely, E., & Zenati, Y. 2018, *A&A*, 619, A53
- Turk, M. J., Smith, B. D., Oishi, J. S., et al. 2011, *ApJS*, 192, 9
- Waldman, R., Sauer, D., Livne, E., et al. 2011, *ApJ*, 738, 21
- Woosley, S. E., Taam, R. E., & Weaver, T. A. 1986, *ApJ*, 301, 601
- Yoon, S.-C., Podsiadlowski, P., & Rosswog, S. 2007, *MNRAS*, 380, 933
- Zenati, Y., Bobrick, A., & Perets, H. B. 2020a, *MNRAS*, 493, 3956
- Zenati, Y., Perets, H. B., & Toonen, S. 2019a, *MNRAS*, 486, 1805
- Zenati, Y., Siegel, D. M., Metzger, B. D., & Perets, H. B. 2020b, *MNRAS*, 499, 4097
- Zenati, Y., Toonen, S., & Perets, H. B. 2019b, *MNRAS*, 482, 1135
- Zhu, C., Chang, P., van Kerkwijk, M. H., & Wadsley, J. 2013, *ApJ*, 767, 164